A segmentation algorithm for characterizing Rise and Fall segments in seasonal cycles: an application to XCO$_2$ to estimate benchmarks and assess model bias

5   Leonardo Calle[1], Benjamin Poulter[2], and Prabir K. Patra[3]

[1] Montana State University, Department of Ecology, Bozeman, Montana 59717, USA

[2] NASA Goddard Space Flight Center, Biospheric Science Laboratory, Greenbelt, Maryland 20771, USA

[3] Japan Agency for Marine-Earth Science and Technology (JAMSTEC), Yokohama, 236-0001, Japan

10   *Correspondence to*: Leonardo Calle (leonardo.calle@montana.edu)

Abstract. There is more useful information in the time series of satellite-derived column-averaged carbon dioxide (XCO_2) than is typically characterized. Often, the entire time series is treated at once without considering detailed features at shorter timescales, such as non-stationary changes in signal characteristics - amplitude, period, and phase. In many instances, signals are visually and analytically differentiable from other portions in a time series. Each *Rise* (increasing) and *Fall* (decreasing) *segment*, in the seasonal cycle is visually discernable in a graph of the time series. The Rise and Fall segments largely result from seasonal differences in terrestrial ecosystem production, which means that the segment's signal characteristics can be used to establish observational benchmarks because the signal characteristics are driven by similar underlying processes. We developed an analytical segmentation algorithm to characterize the Rise and Fall segments in XCO_2 seasonal cycles. We present the algorithm for general application of the segmentation analysis and emphasize here that the segmentation analysis is more generally applicable to cyclic time series.

We demonstrate the utility of the algorithm with specific results related to the comparison between satellite- and model-derived XCO_2 seasonal cycles (2009-2012) for large bioregions on the globe. We found a seasonal amplitude gradient of 0.74-0.77 ppm for every 10° degrees of latitude for the satellite data, with similar gradients for Rise and Fall segments. This translates to a south-north seasonal amplitude gradient of 8 ppm for XCO_2, about half the gradient in seasonal amplitude based on surface site in-situ CO_2 data (~19 ppm). The latitudinal gradients in period of the satellite-derived seasonal cycles were of opposing sign and magnitude (-9 days/10° latitude for Fall segments, and 10 days/10° latitude for Rise segments), and suggests that a specific latitude (~ 2° N) exists which defines an inversion point for the period asymmetry. Before (after) the point of asymmetry inversion, the periods of Rise segments are less (greater) than the periods of Fall segments; only a single model could reproduce this emergent pattern. The asymmetry in amplitude and period between Rise and Fall segments introduces a novel pattern in seasonal cycle analyses, but while we show these emergent patterns exist in the data, we are still breaking ground in applying the information for science applications. Maybe the most useful application is that the segmentation analysis allowed us to decompose the model biases into their correlated parts of biases in amplitude, period, and phase, independently for Rise and Fall segments. We offer an extended discussion on how such information on model biases and the emergent patterns in satellite-derived seasonal cycles can be used to guide future inquiry and model development.

KEYWORDS: GOSAT, DGVM, segmentTS, time series analysis, land use change, seasonal cycle

1. Introduction

Most of our understanding about atmospheric CO_2 dynamics has come from CO_2 sampled by in-situ flask samples or eddy-flux towers at Earth's surface (Ciais et al., 2014). While these data streams have proved incredibly useful, the transient dynamics of fluxes simulated by global-scale terrestrial models have only been compared to a relatively few locations on Earth. In contrast to surface CO_2 samples, which sample CO_2 concentrations in the planetary boundary layer, satellite observations of CO_2 are made by downward-looking Fourier spectrometers from the top of the atmosphere and represent an integrated estimate of CO_2 concentrations in a full column of atmosphere, hereafter 'XCO$_2$' (Wunch et al., 2011; Crisp et al., 2012). Although fluxes from the surface have a large influence on the total column CO_2, the vertical and horizontal transport of air masses in higher atmospheric layers, each with different concentrations CO_2, also influences the CO_2 concentrations in the total column (Belikov et al., 2017), including that of the stratosphere (Saito et al., 2012).

The synoptic coverage and integrated nature of XCO$_2$ means that surface fluxes from around the globe impart information into the seasonal dynamics and inter-annual variability of regional seasonal cycles, which is both a confounding and useful property for evaluating large-scale models. The integrated nature of the data also means that even a few years of data will be sufficient to evaluate the simulated dynamics of global-scale models. We propose that if models can reasonably simulate the timing and magnitude of terrestrial surface fluxes in all bioregions, then we would expect that the simulated XCO$_2$ would match reasonably well with the seasonal dynamics from the benchmark satellite data. Such demonstrated ability could strengthen confidence in regional-to-global model simulations.

To gain insight into seasonal cycle dynamics of satellite XCO$_2$ and individual model behavior, we demonstrate a novel approach to extract more information from the seasonal cycle than is typically characterized. In evaluations of model performance, traditional performance statistics (root-mean-squared-error, correlation, standard deviation) are used to quantify bias in phase and amplitude of the seasonal cycle against a benchmark signal (Coupled Model Intercomparison Project (CMIP) Earth System Models *in* Glecker et al., 2008; DGVMs *in* Anav et al., 2015). In almost all applications, however, the entire time series is treated at once without considering detailed features at shorter timescales, such as non-stationary changes in amplitude, magnitude, period, or phase (Fig. 1). We suggest that traditional performance statistics be applied to categories of unique patterns in the seasonal cycle, and not to the entire time series, thereby characterizing the error structure in a manner that can relate temporal dynamics (amplitude, magnitude, phase) with unique underlying processes.

We extend and apply a time series segmentation method (Ehret and Zehe, 2011) to extract the Rise and Fall segments in seasonal cycles of satellite-derived and simulated XCO$_2$, based on a suite of terrestrial ecosystem models. The advantage of the segmentation approach is that it allows an error structure to be accurately characterized by separately calculating the errors in amplitude, period and phase for each segment type (Rise, Fall). For example, in a graph of a multi-year seasonal cycle of XCO$_2$ (Fig. 1), each *increasing* and *decreasing* segment is visually discernable and analytically differentiable from other portions in the seasonal cycle; hereafter, *Rise* refers to increasing segments and *Fall* refers to decreasing segments in a seasonal cycle. The Rise and Fall segments largely result from seasonal differences in the onset and cessation of terrestrial ecosystem production (Keeling et al., 1995),

which means that a segment's signal characteristics (i.e., amplitude, period, phase) are likewise influenced by different stages of terrestrial ecosystem activity. By segmenting the time series into similar component signals, we can then test for differences in the signal characteristics of Rise and Fall patterns and provide insight into a model's ability to recreate these features of the seasonal cycle over multiple years.

Our first aim was to simply characterize the satellite-derived XCO_2 seasonal cycles in terms of Rise- and Fall-type segment variation. Secondly, we evaluated if signal characteristics and model biases differed or were correlated among Rise and Fall segments, which would help provide information in the missing parts of the satellite-based time-series (i.e., at high latitudes during boreal winter and in the Tropics during the wet-season), which we demonstrate is possible. We also evaluated if model biases between Rise and Fall segments differed enough to provide information about the underlying model representation of terrestrial dynamics, which we underscore as possible but discuss the limits for inference in this regard. Lastly, we explored how a single modeled process (land use and land cover change; LUC) manifests in the different signal characteristics and biases in Rise and Fall segments. We offer discussion on how the segment-based model biases and emergent patterns in satellite-derived seasonal cycles can be used to guide future inquiry and model development.

2. Methods

2.1 Satellite XCO_2 data

Satellite observations of XCO_2 were obtained from the Greenhouse gases Observing SATellite (GOSAT; version 7.3). Onboard the satellite, a Fourier-transform spectrometer measures the thermal and near-infrared absorption spectra of the constituent atmospheric gases within the footprint of observation (~10 km). Satellite data was freely obtained and analyzed only for 2009-2012 because it corresponded to the overlapping timeframe of available simulation data. The data were downloaded from NASA Goddard Earth Sciences (GES) Data and Information Services Center (DISC) online repository (<https://oco2.gesdisc.eosdis.nasa.gov/data/GOSAT_TANSO_Level2/ACOS_L2_Lite_FP.7.3/>; accessed 25 April 2018). We used the Level-2 *Lite* data products, which include only high-quality and bias-adjusted data points, based on the Atmospheric CO_2 Observations from Space (ACOS) retrieval algorithm version 7.3 (Crisp et al., 2012; O'Dell et al., 2012).

A note that satellite data have uncertainties of their own based on instrument noise, version of retrieval algorithm used to filter atmospheric effects, and averaging kernels (Yoshida et al., 2011; Lindqvist et al., 2015). We made the assumption that averaging kernel has a minimal effect on extracted seasonal cycles and we did not apply averaging kernels to the simulation data in this study. A full quantification of uncertainty in satellite-derived seasonal cycles is beyond the scope of this study, but such an analysis could be useful for benchmarking purposes as models continue to reduce large biases (>> 1.0 ppm). Nevertheless, we make the assumption that lower biases are generally indicative of better model performance.

2.2 Simulated Terrestrial Fluxes from DGVMs

The Net Biome Exchange (NBP) from land-to-atmosphere was simulated by six terrestrial ecosystem models (Table 1) that were part of the TRENDY model inter-comparison project version 2 (Sitch et al., 2015; dgvm.ceh.ac.uk). We use the atmospheric convention and make fluxes to the atmosphere positive, and fluxes to the land negative. We

115   assumed that the primary modes of seasonal variability in terrestrial NBP at large scales is described by three terms, Net Ecosystem Production (Net Primary Production – Heterotrophic Respiration), fluxes from fire, and land use change (LUC). The protocol for the DGVM inter-comparison standardized the (i) forcing data: gridded (0.5°) climate (air temperature, short- and long-wave radiation, cloud cover, relative humidity and precipitation), global annual mean CO_2; and the (ii) initial conditions for time-varying simulations for the past century (1860-2012). We

120   used simulated NBP for two sets of model simulations, one where land use (natural vegetation, crop, and pasture fractional cover) is fixed at values from the year 1860 ('S2' scenario described *in* Sitch et al., 2015), and another simulation where land use change is simulated according to the HistorY Database of the global Environment (HYDE v3.1; Goldewijk et al., 2011) ('S3' scenario as described *in* Sitch et al., 2015); both simulation types were forced with time-varying climate and CO_2.

125   **2.3 Fossil Fuel and Ocean Fluxes**

The modes of variability (trend, seasonality, intra- and inter-annual variability) in XCO_2 are also influenced by fluxes from oceanic exchange, fossil fuel consumption and cement production. We used a simplified model of oceanic CO_2 exchanges from Takahashi et al. (2009), and monthly-mean fossil fuel emissions from the European Commission's Emissions Database for Global Atmospheric Research (EDGAR v. 4.2), based on country-level

130   reporting and emissions factors, and the Fossil Fuel Data Assimilation System (http://edgar.jrc.ec.europa.eu/).

2.4 Simulated XCO_2 using an Atmospheric Model

Simulations of atmospheric CO_2 were conducted for the period of 2009-2012 using the land, ocean, and fossil fuel fluxes. We used the Center for Climate Systems Research/National Institute for Environmental Studies/Frontier Research Center for Global Change (CCSR/NIES/FRCGC) AGCM-based chemistry transport model (ACTM)

135   (Patra et al., 2009). The ACTM was run at a horizontal resolution of T106 (~1.125° X 1.125°), and 32 sigma-pressure vertical levels. The simulated XCO_2 values were obtained by taking the sum of the pressure-weighted CO_2 concentrations over all vertical layers, equivalent to the column-averaged observations. We then used 'co-location' sampling of the ACTM XCO_2 data to match the location and timeframe (13:00 hr local time) of observations, ± 5 days to account for (i.e., by averaging) sub-weekly transport errors (Guerlet et al., 2013). We obtained the simulated

140   XCO_2 for each component flux (land, fossil fuel, ocean) and finally summed the components to get the XCO_2 used in bias evaluations.

2.5 Extraction of XCO_2 Seasonal Cycles

We first estimated the mean of daily XCO_2 values by averaging gridded values within each of the 11 TransCom region (Fig. 2), for both the observed and modeled XCO_2. This procedure was as straight forward as written above,

145   and the accompanying computer code (software: R for Statistical Computing) is provided as additional

Supplementary Material. We then applied a digital filtering algorithm (*ccgcrv* by Thoning et al., 1989; https://www.esrl.noaa.gov/gmd/ccgg/mbl/crvfit/crvfit.html) to the mean time series to extract the long-term trend and seasonal cycles, fitted as a 2-term polynomial (linear growth rate was used because the time series spanned only 3 years) and a 4-term harmonic function to account to seasonal asymmetry. Temporal data gaps were linearly

150 interpolated by the algorithm. After subtracting the long-term trend and seasonal cycle, the *ccgcrv* algorithm filters the residuals in the frequency domain using a Fast-Fourier Transform (FFT) algorithm to retain short- and long-term interannual variation (additional details in Nakazawa et al., 1997; Pickers and Manning 2015). The cutoff for the short-term filter was set at the recommended value of 80 days (Thoning et al., 1989). The short-term cutoff of 80-days retains data variations that are evident, or maintained, for the time scale of 3-4 months (4.56 cycles/yr). The

155 cutoff for the long-term filter was set to a large number (3000), which is longer than the number of days in our time series (365 days/yr * 3 yr= 1095 days) because, with such a short time series, we needed to force the estimation of a linear trend with no interannual variation; otherwise, the algorithm would be too sensitive and derive variation in the trend without practical justification. For all analyses here forth, we combined the seasonal cycle with the digitally filtered short-term variation and used the derived data points along the smoothed seasonal cycle curves for analysis.

160 **2.6 Technical description of algorithm: Segmentation of seasonal cycles**

The purpose of this section is to describe the technical algorithms used in the analysis. These algorithms are based on concepts put forth by Ehret and Zehe (2011), translated herein to the R computing language (R Development Core Team, 2008). Where Ehret and Zehe (2011) focused on the single hydrological events, we modify and restructure the algorithm to accommodate much longer non-stationary cyclic time series for general application to

165 seasonal cycle analyses. An R package for the segmentation algorithm is freely available at the GitHub repository <https://github.com/lcalle/segmentTS>. A permanent version of the code is available in the Dryad Digital Repository <doi:10.5061/dryad.vk8ms62>. The computer code is annotated and provides data used in this study with demonstrations for applying the algorithm to remove local minima or maxima and the categorization of seasonal cycle segments.

170 **2.6.1 Categorize segments and isolate seasonal Rise and Fall cycles**

We first determine the first derivatives numerically. The *ccgcrv* signal decomposition algorithm outputs a daily time series in the form of a multi-dimensional array, but we focus on a subset of the array, the 2-dimensional rectangular matrix representing points along the detrended seasonal cycle,

$$\boldsymbol{B} = \begin{bmatrix} b_{1,1} & b_{1,2} & b_{1,3} \\ \vdots & \vdots & \vdots \\ b_{n,1} & b_{n,2} & b_{n,3} \end{bmatrix} \tag{1}$$

175 , where the first column is the row index, the second column are dates, the third column is the detrended XCO_2 ppm with the short-term variation added back-in, the rows are the triplets of the index, time in the x-direction, and magnitude (XCO_2 ppm) in the y-direction.

We can numerically determine the first derivative in the y-direction at each point via differencing, as in,

$$\nabla b_{i,2} = b_{i,2} - b_{i-1,2} \tag{2}$$

180   We then classifying each row in first column ($b_{i,2} \dots b_{n,2}$) into one of the following categories below and expand **B** to a $n \times 4$ matrix to store the classified values. The main objective is to classify the endpoints (Trough, Peak) of the Rise and Fall segments:

$$\forall i \in \{1 \dots n\}, \ \mathbf{b_{i,4}} = \begin{cases} Trough, & (\nabla b_{i,2} < 0) \wedge (\nabla b_{i+1,2} > 0) \\ Rise, & (\nabla b_{i,2} < 0) \wedge (\nabla b_{i+1,2} < 0) \\ Fall, & (\nabla b_{i,2} > 0) \wedge (\nabla b_{i+1,2} > 0) \\ Peak, & (\nabla b_{i,2} > 0) \wedge (\nabla b_{i+1,2} < 0) \\ Null, & otherwise \end{cases} \tag{3}$$

We then take the subset of endpoints (S) in the classified matrix **B**,

185    $$S \subset \mathbf{B} = \{\mathbf{B} \mid \mathbf{b}_{i,3} \text{:} \ Trough, Peak \tag{4}$$

, where S retains the dimensions of the **B**. A unique segment (s) is defined as a set of two consecutive endpoints (rows) in S that alternate in their classification of Trough or Peak, meeting the condition:

$$s \subset S = \{S \mid (S_{i,4}\text{:} Trough \ \wedge \ S_{i+1,4}\text{:} Peak) \vee (S_i\text{:} Peak \ \wedge \ S_{i+1,4}\text{:} Trough) \tag{5}$$

    We identify local minima and maxima that are deviations in otherwise longer (seasonal) and more general

190   Rise and Fall patterns based on two criteria below, and then reclassify the segments based on the class of the segment with the largest amplitude. The amplitude of a segment (a_s) is defined as:

$$a_s = |s_{1,2} - s_{2,2}| \tag{6}$$

, where $s_{1,2}$ is the first endpoint in the second column (XCO2 ppm), either a Trough or a Peak, and $s_{2,2}$ is the second endpoint for the specific segment, which, by definition the first endpoint must be classified ($s_{1,4}$) as one of Peak or

195   Trough and must not have the same classification as the second endpoint ($s_{2,4}$).

    The first criterion sets a minimum threshold for the amplitudes, redefining the set of endpoints defining the segments, as below:

$$s^* \subset s = \{s \mid a_s > \ minimum \ threshold \tag{7}$$

    Segments that represent local minima or maxima that are not of interest to the user can be identified by a

200   comparison of amplitudes of consecutive segments, dropping the segment with the lowest amplitude, as below:

$$s^{*\prime} \subset s^* = \{s^* \mid s^* \neq min(a_{s-1}, a_s, a_{s+1}) \tag{8}$$

This procedure results in a new subset of segment endpoints ($s^{*\prime}$) with consecutive elements that have similar classification (e.g., $s^{*\prime}_{1,4} \coloneqq Peak$, and also, $s^{*\prime}_{2,4} \coloneqq Peak$), which needs to be rectified. We keep the endpoints with the lowest *Trough* value and the largest *Peak* value,

205    $$s[t]^* \subset \begin{cases} s[t]_{1,2} & s[t+1]_{1,2} \\ s[t]_{2,2} & s[t+1]_{2,2} \end{cases} =$$

$$\begin{cases} s[t]^*_{1,2} = \begin{cases} min\big(s[t]_{1,2}, s[t+1]_{1,2}\big), & s[t]_{1,4} \coloneqq Trough \wedge s[t+1]_{1,4} \coloneqq Trough \\ max\big(s[t]_{1,2}, s[t+1]_{1,2}\big), & s[t]_{1,4} \coloneqq Peak \quad \wedge s[t+1]_{1,4} \coloneqq Peak \end{cases} \\ s[t]^*_{2,2} = \begin{cases} min\big(s[t]_{2,2}, s[t+1]_{2,2}\big), & s[t]_{2,4} \coloneqq Trough \wedge s[t+1]_{2,4} \coloneqq Trough \\ max\big(s[t]_{2,2}, s[t+1]_{2,2}\big), & s[t]_{2,4} \coloneqq Peak \quad \wedge s[t+1]_{2,4} \coloneqq Peak \end{cases} \end{cases} \tag{9}$$

, where $s[t]$ is a unique segment in the set of s segments, $s[t+1]$ is the following consecutive segment, $s[.]_{1,2}$ and $s[.]_{2,2}$ are the segment first and last endpoints, respectively, and $s[t]^*$ is the updated segment with new endpoints $s[t]^*_{1,2}$ and $s[t]^*_{2,2}$, while segments $s[t], s[t+1]$ have been removed from the set of segments (s).

210   A (subjective) limit can also be set to exclude or include segments based on temporal proximity. For example, consecutive minima (*minima*/maxima/*minima*) should not be considered local minima if separated by 365 days; these are probably real local minima driven by processes unique to different seasons. By contrast, local minima separated by 60 days may represent signals within the overall seasonal Rise and Fall pattern (e.g., due to fire). For this study, we are more interested in assessing the general seasonal patterns. We therefore estimate the temporal

215   distance, in 'days' (D_s), between the first endpoints of consecutive segments and evaluate the condition as below,

$$D_s = s[t+1]_{1,3} - s[t]_{1,3} \text{, given } s[t]_{1,4} \land s[t]_{1,4} \text{ are of the same class } (Trough, Peak) \qquad (10)$$

$$s^* \subset s = \{s \mid D_s > \text{ minimum threshold} \qquad (11)$$

, where $s[.]_{1,3}$ is the endpoint date in the x-direction, and the minimum threshold for distance between endpoints is set at a conservative 250 days (~8 months), ensuring that only the main Rise and Fall patterns within a given year

220   are captured. This conditional evaluation also results in a new subset of segments (s^*) with consecutive elements with similar classification, as above, but Eq. 9 can be re-applied to select the endpoints which represent general Rise and Fall patterns.

       Additional criteria can be applied to automate the removal of local minima/maxima that are not relevant to the user, but we caution that visual inspection of the signal is important to avoid unwanted reclassification of segments

225   in the time series.

2.6.2 Human-assisted pattern recognition via visual inspection

The procedure outline in Sect. 2.6.1, above, is applied to both the reference (R) and modeled (M) seasonal cycle time series. In the best of cases, the procedure would result in matrices for R and M, each with an equal number segments and the same sequence of endpoint classes (*Trough, Peak, Trough, Peak, ...*). In practice, however, the number and

230   sequence of segments in M will not always equal the number or sequence of segments in R. When variability in the modeled seasonal cycle results in many local minima/maxima, and therefore many short Rise/Fall segments, there can be a mismatch between the indices of segments, wherein smaller/shorter segments in M are matched to much larger/longer segments in R; this is simply an artefact from automation of the procedure outlined previously. Although we have implemented automated procedures in the algorithm that reconcile these types of mismatches, we

235   found that it was considerably quicker to (*i*) conduct a 'blind' run of the algorithm on the data, (*ii*) visually inspect the automated graphical plots of the seasonal cycles for mis-matching segments (Supplementary Material Fig. S1), (*iii*) identify the index of the mis-matching endpoints in M, and then finally (*iv*) re-run the algorithm specifying the index of the endpoint in M for removal.

2.6.3 Segment signal characteristics and error statistics

240   The amplitude (Eq. 6) and period (*p* in 'days') for all segments are first characterized, with the period defined as,

$$p_s = s_n - s_0 \qquad (12)$$

, where s_n and s_0 are the end and start dates of a segment, respectively. Then, for each segment in M and R, a complementary vector Mx and Rx is created in the x-direction with a fixed number of, and equally-spaced, dates,

$$x = (x_1 \ldots x_k) \qquad (13)$$

245 Each element in Mx corresponds, by index, to an element in Rx, such that a matching pair exists. Similarly, a complementary vector My and Ry is created in the y-directions, with the length of the vector matching the length of the vector in the x-directions (k). For each element in My and Ry, we perform a linear interpolation of the values of XCO_2 ppm in **B** (**b.,2**) for the indices given by the dates in Mx and Rx; fortunately, the linear interpolation is automated by the *approx* function in R, which makes this procedural step straightforward. The end result is, for

250 every segment in M and R, four vectors of equal length in Mx, My and Rx, Ry, with the timing of the data and values of XCO_2 ppm that follow the corresponding seasonal cycles in **B**. We can then decompose the corresponding errors in phase and magnitude along the time series,

$$Timing\ error = Mx - Rx \qquad (14)$$

$$Magnitude\ error = My - Ry \qquad (15)$$

255 Although in this paper we focus only on errors in amplitude, period, and phasing of the segments, the time series of errors in timing and magnitude are an additional level of detail in the error structure that is evaluated by the segmentation algorithm.

2.7 Statistical summaries

For each of the Rise and Fall segments within a region, we summarized the characteristics by averaging the
260 amplitude (ppm), period (days), and the phase, which we estimated in two ways based on the day of year for the first and last endpoint of the corresponding segment (DOYstart, DOYend, respectively). For model biases, we used the total sum of the component tracers (land + fossil fuel + ocean) and we summarized model biases as the region-average of segment-to-segment differences between model and observation. Although we aggregate the biases among segment types, and therefore lose information, we do this to demonstrate that there are distinct general
265 patterns in the Rise and Fall segments, regardless of region. Of course, one might be more interested in one bioregion over another, and while this is indeed possible and suggested, such analysis is not the intent of this paper.

The latitudinal variation of amplitude and period length for Rise and Fall segments was evaluated by comparing the regionally-averaged metrics against the average latitude of each TransCom region. We sought to evaluate a model's ability to reproduce the north to south gradient in seasonal cycle characteristics. We also use data from in-
270 situ [CO2] flask samples for 2005-2015 (NOAA/ESRL/GMD CCGG cooperative air sampling network; https://www.esrl.noaa.gov/gmd/ccgg/flask.php) as a check to evaluate latitudinal variations of surface site seasonal amplitudes. Surface sites were selected if they had a minimum of five years of data between 2005-2015, with at least one flask sample per month. The peak-trough amplitude was then taken from monthly averaged data. Linear correlations were deemed statistically significant at levels of p=0.05.

275 The amplitude and period length asymmetries between Rise and Fall segments were calculated as in the following example. Given a sequence of data with segments of type {*Fall_1*, *Rise_1*, *Fall_2*, *Rise_2*}, representing seasonal cycles over two years, three asymmetries in amplitude and period length would be calculated for the sequence of segments, as (*i*) Fall_1 - Rise_1, (*ii*) Fall_2 - Rise_1, and (*iii*) Fall_2 - Rise_2. The asymmetries are referenced to Fall segments such that, for example, negative asymmetries mean that the amplitude (or period length)
280 is greater in the Rise segment. The reason we calculated asymmetries between segments immediately before and

after the Fall segments is because we assumed that there is some degree of autocorrelation in the relational values that is both real and could provide useful information, but the underlying causal mechanisms are speculative at this point.

2.8 Application of approach

285 We applied the approach to evaluate the effect of LUC on XCO_2 by using the segment characteristics setting the 'S2' scenario as the reference time series and then following procedures outlined in Sect. 2.6 to match corresponding Rise and Fall segments in the S3 and S2 simulations. We then calculated the difference in the amplitude, period, and phase between matching segments, hereafter defined as the 'LUCeffect'. To evaluate the relative influence of the LUCeffect on changes in amplitude, period and phase, we transformed the LUCeffect to percentages by (a) dividing

290 the LUCeffect in amplitude by region-specific average amplitudes, and (b) dividing the LUCeffect in the period length and phase (DOYstart, DOYend) by the region-specific average period lengths. We then pooled the absolute values of the standardized LUCeffects for all regions, by model; the absolute values of LUCeffect was used because we were more interested in any significant change, rather than a directional change in the metric values. We conducted an Analysis of Variance to test for significant differences among models and type of LUCeffect

295 (amplitude, period, and phase), in terms of the percent LUCeffect, also setting significant differences at p=0.05. In this manner, we were able to determine the relative importance of LUCeffect by metric and compare amongst models.

3. Results

3.1 Satellite coverage and XCO_2 seasonal cycles

300 The satellite data coverage had sufficient temporal density to extract smooth seasonal cycles (Fig. 3), except during Boreal Winter at high latitudes (> 50˚ N) and during the wet-season in Tropical Asia where there was clear evidence of linear interpolation over large data gaps (Supplementary Material Fig. S2-S4). We had to exclude North America Boreal and South America Tropical regions from all analyses because the data were too sparse and seasonal cycles could not be derived. The mean number of satellite retrievals per day in 5˚ bins was greater than 1 when averaged

305 over a season, but the spatial distribution of the retrievals by month (Supplementary Material Fig. S2-S4) showed that only portions of the TransCom regions were being represented with satellite observations. The lack of a complete representative sample of satellite observations in a region suggests that the derived seasonal cycle will be biased towards the XCO_2 observations in those sub-regions with greater coverage. We take this finding as a caveat, but also demonstrate below that the derived seasonal cycles are a good representation of the general seasonal

310 dynamics in the data.

There were noticeable deviations (local minimums) from otherwise consistent Rise and Fall patterns during a season (for example in North Africa in Fig. 3). We compared the seasonal cycles derived from DGVM XCO_2 co-located with GOSAT retrievals against DGVM seasonal cycles using all simulated XCO_2 and complete coverage (no-colocation). For the single DGVM studied in this side analysis, the local deviations were still evident in the

315 seasonal cycles that used data with complete coverage (Supplementary Material Fig. S5). We believe that these

deviations are not artefacts of the spatial distribution of satellite retrievals, but instead are true patterns in the XCO_2 seasonal cycle. However, the co-location sampling did appear to have a greater effect on the amplitudes and periods in Southern Hemisphere regions, whereas the effect of co-location sampling was less influential in Northern Hemisphere regions.

320   The magnitude of the GOSAT seasonal cycle residual error, averaged over all regions, was 0.15 ± 1.02 ppm, which was not a small fraction relative to the average amplitudes when taking into account the standard deviation. However, the residuals, were normally and randomly distributed around zero (Supplementary Material Fig. S6), which we took to suggest that there was no systematic bias and that the daily spatial variation in data coverage averaged out, and what we derived was a realistic estimate of seasonal variation in XCO_2.

325   **3.2 Latitudinal variation in XCO₂ seasonal cycle amplitudes**

Seasonal amplitude varied predictably with latitude (Fig. 4). Latitude explained between 82-84% of the variation in seasonal amplitudes in GOSAT, with the range taken from linear models of Rise and Fall segments (Fig. 4). There was an increase in amplitude of 0.74 ± 0.13 ppm ($\mu \pm$ S.E.) for Rise Segments and 0.77 ± 0.13 ppm for Fall Segments for every 10 degrees of latitude for GOSAT. Whereas the XCO_2 amplitudes exhibited a linear relationship
330   with latitude, in-situ flask samples of CO_2 exhibited a log-linear relationship with latitude (Fig. 5; $R^2 = 0.90$, d.f.=45, $p < 0.001$), which indicates larger amplitude gradients at higher than at lower latitudes. The difference results in a latitudinal range (Equator to $70˚N$) in seasonal amplitude of ~7 ppm for XCO_2 (taken as $70˚ * [0.077 + 1.95*0.013]$, as the largest possible amplitude gradient in XCO_2; $\mu + 1.95*$S.E.) and ~17 ppm for surface CO_2. The dampened gradient in XCO_2 amplitude suggests substantial north-south atmospheric mixing, which is consistent with a
335   previous study on the meridional versus zonal contribution to XCO_2 via atmospheric transport (Keppel-Aleks et al., 2012). In addition, the in-situ sampling stations are located in such a way that they sample the 'background' atmosphere, which reduces the influence of local to regional terrestrial fluxes, and instead they provide seasonal cycles representative of hemispheric- and continental-scales. The contrast between the latitudinal gradient in amplitude between XCO_2 in this study and in-situ surface samples may therefore be even greater than reported here
340   (Olsen and Randerson, 2004; Sweeney et al., 2015).

     Only LPX was able to simulate the GOSAT-derived latitudinal gradient (slope) in amplitude, but even in this model, the magnitudes of the amplitudes were consistently lower than GOSAT by ~1.5 ppm (Fig. 4). ORCHIDEE simulated the latitudinal gradient in amplitude reasonably well and CLM simulated a marginally stronger north-south gradient, whereas the gradient was much weaker in two models (OCN, VISIT) and there was no statistically
345   detectable amplitude gradient in LPJ. The evidently enhanced meridional mixing of total column CO_2 complicates an interpretation of the finding that most models simulated a weaker gradient in XCO_2 seasonal amplitude (Fig. 4). It makes it difficult to determine why models do not reproduce the latitudinal gradient in amplitude very well – for example, are the magnitudes of the fluxes in certain regions too low or too high, such that they offset the seasonal amplitudes in the region of interest after atmospheric transport? We offer suggestions in the Discussion that might
350   help answer these questions.

     3.3 Latitudinal variation in XCO₂ seasonal cycle period

The period lengths of GOSAT XCO$_2$ seasonal cycles also varied predictably with latitude (Fig. 5) and there was no significant difference in the magnitude of the latitudinal gradients between Rise and Fall segments, although the direction of the gradient was positive for Rise segments and negative for Fall segments (Fig. 4). Latitude explained between 67-73% of the latitudinal variation in period lengths in GOSAT seasonal cycles. From South to North, the period lengths of Rise segments increased by 10 days per 10° of latitude for GOSAT. From South to North, the period lengths of Fall segments had negative gradient and decreased by -9 days/10° latitude for GOSAT. The opposite gradient in period lengths of Rise and Fall segments implies that around 2° N, the period of Rise and Fall segments of equal duration. North of this point of inversion in asymmetry, the period lengths of Rise segments are greater than in Fall segments, with an increasing asymmetry as latitude increases. We hypothesize that the latitude at the point of inversion of period asymmetry is a characteristic indicator global atmospheric dynamics and biosphere productivity. Our rationale is that if (i) the primary driver of the period of drawdown (Fall) or release (Rise) in XCO$_2$ seasonal cycles is the terrestrial biosphere, and (ii) DGVMs themselves simulate the terrestrial biosphere, then variation in the simulated point of inversion of asymmetry by different DGVMs suggests a strong influence of biosphere activity on this emergent pattern. The most obvious driver affecting the period being plant phenology. Furthermore, we already know that seasonal cycle in XCO$_2$ is dominated by flux seasonality in land biosphere, with the ocean and fossil fuel emission seasonality plays only a secondary role. Nevertheless, a north or south shift in the latitude of inversion (i.e., 2° N) would indicate that long-range transport of atmospheric signals, such as the poleward transport of southerly signals (Parazoo et al. 2016), has changed substantially. In which case, the relative contribution of long-range signals from southerly locations to seasonal cycle anomalies (in phase or amplitude) in northerly locations might be greater or less than expected. As of yet, however, it is unclear if this point of inversion is relatively stable over time or if, instead, the point shifts in latitude among years or decades depending on the relative influence of source-sink dynamics in biospheres in the Northern and Southern Hemispheres.

Most models correctly simulated the satellite-derived latitudinal gradient in period, but LPJ and VISIT did not simulate statistically significant gradients in either Rise or Fall segments, and LPX could only reproduce the gradient for Rise segments, but not for Fall segments (Fig. 4). For CLM, OCN and ORCHIDEE, the simulated gradients were statistically similar to GOSAT, although the absolute period lengths differed by up to 25 days. The latitudinal gradient in period of XCO$_2$ seasonal cycles is emergent from the underlying timing and duration of biosphere productivity, and as such, it serves as a high-level constraint on simulated dynamics. It may therefore be possible to add this emergent pattern as a benchmark to evaluate models that attempt to reproduce more direct indicators of biosphere activity, such as seasonal patterns in leaf area (Richardson et al., 2012), or primary production (Forkel et al., 2014).

3.4 GOSAT asymmetries in period and amplitude

The period asymmetry between Rise and Fall segments (Table 2) is clearer when comparing the periods of consecutive Rise and Fall segments (Fig. 6), taking the Fall segment as reference, as described in Sect. 2.7. The period asymmetries were in the same direction except for the Africa Northern, Africa Southern, and South America Temperate regions (Fig. 6A). The asymmetries exhibit stable patterns of consistent direction within many regions,

and they also display quite a bit of interannual variation in the magnitude (or direction in some cases) of the asymmetries themselves (Fig. 6A and 6B). For example, the standard deviation in period asymmetry averaged 11% of the region-averaged periods for GOSAT seasonal cycles, and it was greatest for the Africa Southern region (42%). For context, a 10% change amounts to a change in period asymmetry by 5-29 days, and as much as 73 days in the Africa Southern regions, which is certainly a remarkable change in the atmospheric signal. The period asymmetries can provide insight into the underlying terrestrial dynamics, for example, from interannual variation in the duration of the carbon uptake period (Xia et al., 2015; Fu et al., 2017), but it is yet unclear how changes in carbon uptake period manifest to affect these patterns of asymmetry. Furthermore, one DGVM (ORCHIDEE) was able to simulate period asymmetries, consistent in direction, with that of the GOSAT record when using co-location sampling. Albeit, the magnitude of the period asymmetry for ORCHIDEE was about half that of GOSAT, but it does suggest that the surface fluxes from this DGVM were more realistic in timing and magnitude. All other models had greater interannual variation in the direction of the asymmetry, with no other model reproducing the direction of asymmetry in all regions.

The amplitude asymmetries between consecutive Rise and Fall segments were more variable in the direction of the asymmetry for GOSAT (Fig. 6B). There was no consistent pattern in the direction or magnitude of the amplitude asymmetries within or among regions, but we did not investigate if there were annual patterns that were consistent among all regions. No model successfully reproduced the direction of asymmetry in amplitude across all regions in all years. As of yet, the relevance of interannual variation in the asymmetries is speculative, but we do know that such variation is not simply due to data coverage (Supplementary Material Fig. S5), so there may be more insightful information in the signal.

3.5 Correlated biases between Rise and Fall segments

The correlations of model biases differed more among Northern and Southern Hemispheres (NH and SH, respectively) than among regions, so we present the following analyses not by region, but by NH and SH. The NH regions were comprised of Africa Northern, Europe, Eurasia Temperate, North America Temperate; the SH regions were comprised of Africa Southern, Australia, and South America Temperate. These analyses required data on both Rise and Fall segments, which eliminated the Asia Tropical and Eurasia Boreal regions from these analyses.

Among Rise and Fall segments, and among all models and regions, the model biases in amplitude were nearly perfectly correlated (NH R^2 = 0.99, d.f. = 28, t= 64.63, p < 0.001; SH R^2 = 0.99, d.f. = 16, t = 65.02, p < 0.001; Fig. 7a and 7e). Except for ORCHIDEE and CLM, which exhibited the smallest amplitude biases, the other models all had amplitudes that were too low. In the SH, there was a similar pattern of negative amplitude biases (Fig. 7e), with exception that CLM simulated amplitudes that were too large in two of three SH regions. The strong correlations suggest that knowing the amplitude biases in one part of the seasonal cycle is sufficient to gain information about amplitudes in the missing part of the seasonal cycle. This might be particularly useful for constraining estimates of XCO$_2$ seasonal cycle patterns during timeframes that have poor satellite coverage (Boreal Winter, Tropical Wet Season). Furthermore, it is revealing that models which simulate amplitudes that are too low do so almost equally for both Rise and Fall segments, which is suggestive of a systematic bias in the sensitivity of the models to seasonal

changes in climate. Such systematic biases can be due to simulated fluxes that are overall lower in magnitude, or due to a pattern of spatio-temporal fluxes that end up offsetting or cancelling each other in the atmospheric domain, but we cannot yet definitively attribute the bias of individual models to one of these possible causes.

The average period biases of Rise and Fall segments were also strongly correlated, with a greater strength of correlation in the NH ($R^2 = 0.77$, d.f. = 22, t= -8.53, p < 0.001) than in the SH ($R^2 = 0.82$, d.f. = 21, t = -9.87, p < 0.001). In the NH, almost all models simulated periods that were too short in Rise segments and too long in Fall segments, in approximately equal and opposing amounts (Fig. 7b). In the SH, the period biases spanned both positive and negative values for both of the Fall and Rise segments, but also in approximately equal and opposing amounts of bias (Fig. 7f). There were only a few data points where the periods within a region were either biased (a) too short for Rise segments and also too short for Fall segments, or (b) where the Rise segment was biased too long and the Fall segment also biased too long. These patterns are suggestive of underlying constraints that compensate for biases in periods, such that situation (a) and (b), from above, rarely occur. Such constraints are likely associated with the underlying drivers of the period of Rise and Fall segments. For instance, models that simulate growing seasons that are too long will likely simulate Fall-segment periods that are also too long, and as a consequence, the dormant season will be shortened, as will the periods of associated Rise segments. Within a given model, the magnitude of compensating biases varied by region, so it is possible that biases in biosphere activity varied similarly by region. To incorporate such insights will require direct manipulation of the phenology represented by models, but improving the emergent patterns in period to better match the satellite-derived XCO_2 seasonal cycles will bolster confidence in the model's ability to represent both fine-scale dynamics and the emergent large-scale atmospheric patterns.

3.6 Application of Approach: LUCeffects on amplitude, period and phase metrics were non-trivial

We describe the LUCeffect as the percent change in the Rise and Fall segment amplitude, period, and phase (DOYstart, DOYend) when LUC processes are included in model simulations, relative to seasonal cycle metrics when LUC was not included in simulations. Among all models and Rise and Fall segments, the average LUCeffect was largest on amplitude (mean 13.4%, or 0.37 ppm), but there were also non-trivial changes in the period (7.2%, or 13.2 days), and phase metrics of the DOYend (6.5%, or 11.4 days) and DOYstart (6.2%, or 11.4 days). An Analysis of Variance suggested that the LUCeffects did not significantly differ between Rise and Fall segments (F= 0.006, d.f.=1, p = 0.941), and that the specific model explained 16% of the variation (F= 15.183, d.f.=5, p < 0.001) and the metric explained only 5% of the variation (F= 7.815, d.f.=3, p < 0.001). LPJ was an outlier in that it simulated larger LUCeffects in every metric (mean LUCeffect=18%), approximately 8% greater than other models. The remaining variation in LUCeffect was explained by the larger LUCeffect on amplitude in LPX and VISIT (Fig. 8), whereas OCN simulated only marginally greater LUCeffects than CLM and ORCHIDEE. The LUCeffects were of similar magnitudes as the baseline interannual variation for these metrics, in terms of percent change, or greater in the case of the LUCeffect on amplitude (Table 3).

The importance of the LUCeffect on the amplitude of Rise and Fall segments was somewhat expected because LUC directly affects the type of land cover simulated in the models, for example, by converting forest to pasture or

460 pasture to forest and thereby influencing the magnitude of surface fluxes directly (Arneth et al., 2017). However, the effect of LUC on the temporal metrics of the seasonal cycle (period, phase) is typically understated in the literature. The LUCeffects on period and phase are of the same relative magnitude as is observed in two-decades of advancement in the start and end dates of the carbon uptake period based on atmospheric inversion studies (Fu et al., 2017). It should not be a surprise then that LUC can affect the timing of surface fluxes, but this facet is often

465 overlooked when the focus is solely on variability at annual or decadal timescales. At the very least, this work shows that land-surface modelers should consider the impact of LUC on the timing and duration of surface fluxes, in addition to its effect on the magnitude of the fluxes.

4. Discussion

4.1 Utility of a segment analysis for analyzing cyclic time series

470 We demonstrated that a segmentation analysis of satellite-derived XCO_2 seasonal cycles can generate direct estimates of amplitude, period, and phase at global and hemispheric scales, and that it can reveal stable patterns in the metrics which can be used as benchmarks to evaluate simulation models. There is obvious value in using standard statistics (RMSE, S.D., R^2, etc.) to characterize a time series and evaluate it against simulated reproductions (e.g., 'Taylor diagrams'; Taylor, 2001; Supplementary Fig. S7). We do this too, but we argue that

475 applying statistical measures of goodness-of-fit over the entire time series misses an opportunity to extract valuable information from observational data and provide more direct measures of bias. Studies that have evaluated amplitude and period biases directly have been based on the mean harmonic of the seasonal cycle (Peng et al. 2015), which lacks interannual variation, and therefore does not fully represent the modeled biases. Furthermore, the metrics for the asymmetric Rise and Fall patterns in seasonal cycles are not typically estimated, nor evaluated for

480 bias. In the Europe region, for example, the internanual variation in amplitude (1.25 ppm) and period (25 days) is certainly not trivial (Supplementary Fig. S8), and if excluded in evaluations it would cause a biased assessment of what the models can and cannot do well, limiting the potential of such assessments to inform potential improvements.

Our study focused on the Rise and Fall segments in XCO_2 seasonal cycles, corresponding to periods when

485 terrestrial ecosystems generally release and uptake carbon dioxide, respectively. Other studies might be more interested in shorter-term, pulse-type signals, such as the ability of models to simulate the effect of large scale fires or volcano eruptions in an atmospheric time series. In either case, the segmentation algorithm could help standardize and decompose model bias into its component parts of amplitude, period and phase biases.

4.2 Asymmetries provide new insights into the interannual variation of atmospheric signals

490 By definition, the asymmetries (Fig. 6) are not anomalies, but similarly, the amplitude asymmetries are directly related to underlying processes generating the imbalance in the amplitude and period between Rise and Fall segments. Most likely, the asymmetries reflect the difference in the magnitude or in the timing of fluxes during the growing season for Fall segments and phenological dormancy for Rise segments (Randerson et al., 1997). Whereas the signature of the terrestrial biosphere may be a more dominant driver of the period asymmetries, the amplitude

495   asymmetries may also be influenced by processes that the models simply do not simulate well, or in any sufficient manner in some cases, such as sub-seasonal representation of Fire and LUC (Earles et al., 2012) or volcano eruptions (Jones and Cox, 2001). The interannual variation in XCO_2 period and amplitude asymmetries are directly related the activity of terrestrial ecosystems, but questions remain – are the annual asymmetries in amplitudes or periods evident of a global response to large-scale climate phenomena, such as the El Niño-Southern Oscillation?

500   Do some regions dominate and influence the signal more than others? To what degree do the asymmetries in one region provide information about asymmetries in other regions, and can we infer dynamics in Boreal regions, for example, by analyzing atmospheric signals in regions where satellite coverage is more complete? The asymmetries offer a new level of information on atmospheric dynamics that is ripe for exploring.

4.4 The effect of LUC on seasonal cycles is in addition to the effect on the long-term trend

505   Much focus has been put on accurately characterizing component fluxes from land use and land cover change simulated by DGVMs (Pongratz et al., 2014; Calle et al., 2016), but we also show that LUC influences the atmospheric seasonal cycle period and phase at a level that is comparable to the reference rates of interannual variation in those metrics (Table 3). This underscores a complex problem of trying to simultaneously resolve the contribution of LUC fluxes to the long-term trend in atmospheric CO_2 (Le Quéré et al., 2018), and also to represent

510   realistic LUC effects on seasonal-scale biosphere activity (Betts et al., 2013; Bagley et al., 2014). For instance, when land is converted from forest to pasture, the dominant land cover will affect the duration and timing of the surface fluxes (Fleishcher et al., 2016) and this seems obvious on its own standing. However, DGVMs were not developed during the era of satellite XCO_2 observations, and so the main issue of trying to resolve the effect of large-scale changes in land use on both the long-term trend and seasonal cycle dynamics is not easily solved. But now that these

515   data are available, perhaps a new approach is necessary to take advantage of these large-scale benchmarks.

        The inclusion of LUC in the simulations, after including the contribution from fossil fuels and ocean, resulted in a combined long-term trend estimate which was too large, by 0.07 to 1.72 ppm yr^{-1}, compared to the long-term trend of GOSAT XCO_2 (2.16 ± 0.01 ppm yr^{-1}) (Supplementary Fig. S9). The GOSAT estimate is comparable to an independent estimate of the long-term trend of XCO_2 from SCIAMACHY for the 2000s ($1.95 \pm$

520   0.05 ppm yr^{-1}; Schneising et al., 2014). If we assume that this study's simulated long-term trends of fossil fuel fluxes (4.44 ± 0.008 ppm yr^{-1}) and those of the ocean (-0.66 ± 0.0006 ppm yr^{-1}) are better constrained than the trends from the land fluxes, then according to the GOSAT benchmark, the simulated land sink is too weak. Despite the posibility that these simulated LUC fluxes are too high, the DGVM versions applied in this study do not simulate a suite of land management processes (shifting cultivation, wood harvesting, pasture harvest, agriculture mgmt.) that

525   have been shown to increase the annual LUC flux by 20-60% (Arneth et al., 2017), further pointing to a simulated land sink that is too weak. DGVM-based estimates of the terrestrial land sink have been compared against a residual term in the global carbon budget that is taken as the average flux over a decade (Le Quéré et al., 2018), but perhaps we are overlooking something here. The cumulative fluxes simulated by the models in this study (from 2002-2012) resulted in a long-term trend that is at odds with the satellite record, and it is unclear why. We must therefore

530   attempt to reconcile biases in both the long-term trend and seasonal cycle dynamics if we are to use XCO_2, or other

integrated atmospheric measurements to constrain model dynamics, and not simply assess these patterns independently.

4.5 Caveats, limitations and ways forward

The XCO_2 gradient in amplitude is approximately half the gradient in amplitude of in-situ surface CO_2. The
535   dampened XCO_2 gradient suggests the presence of strong meridional mixing, which complicates accurate attribution of model biases to any specific bioregion. In effect, the XCO_2 seasonal cycle is comprised of the fluxes from all regions to varying degrees (Olsen and Randerson, 2004; Sweeney et al., 2015; Lan et al., 2017). Given this, simulating the atmospheric transport of the surface fluxes from all regions at once would allow us to both, (a) obtain useable estimates of model bias and (b) to provide attribution to those biases. Indeed, the model biases were fully
540   described, but only in terms of XCO_2, not in terms of terrestrial surface fluxes themselves. An approach for attribution of model bias in XCO_2 might be laid out similar to Liptak et al. (2017), wherein the surface fluxes from each region (by year) undergo independent atmospheric transport. In a framework similar to this study, such simulations might prove instrumental in determining the fractional contribution of each region's fluxes the XCO_2 seasonal cycle characteristics while also providing better guidance for model development.

545   Model evaluations also showed that few models have low bias in all seasonal cycle metrics of amplitude, period, and phasing of simulated XCO_2. An inherent requirement for reproducing the XCO_2 signal is that the land-to-atmosphere fluxes are reasonable in magnitude, duration and timing *in all land regions*, or at the very least, in land regions with large vegetative areas that might disproportionately dominate the signal. Even though such requirement may be necessary to simulate the amplitude asymmetries, this is an extreme level of proficiency that,
550   simply, the models do not currently exhibit.

        Lastly, the relative contribution of land, ocean and fossil fuel fluxes to the seasonal cycle differs by region, latitude, and time period (Randerson et al., 1997). This poses some concern because fossil fuel and cement fluxes are considered to have low uncertainty, but they may be biased too high in some regions (Saeki and Patra 2017), affecting our interpretation of the contribution of simulated land fluxes to the seasonal cycle amplitudes, especially
555   if the fossil fuel seasonal cycle signal is additive to (or offsets) the signal from the land fluxes. Other land uncertainties were not addressed in this study as it was not our intent to determine which DGVM had zero bias. Instead, we sought to extract unique patterns in the observed signals so that they may inform model development and subsequent evaluations in the future. Model improvements in their representation of important land processes such as forest demography, wetland and permafrost dynamics, agriculture and land management, and a greater
560   diversity of functional plant diversity are all on the horizon (Pugh et al., 2016; Fisher et al., 2018) and may further improve simulated atmospheric signals. The patterns in XCO_2 seasonal cycles are emergent from surface fluxes over the globe, and we foresee that a segment-based analysis of atmospheric seasonal cycles as a way to extract emergent patterns in the reference data to help guide future development and an improved understanding of the terrestrial biosphere.

565   **Acknowledgements**

We thank Ehret and Zehe (2011) for their initial foray into alternative approaches to automate pattern matching in time series, which inspired this study. We thank the TRENDY Version 2 DGVM modelling community for their extensive efforts in continuing to advance model representation and making simulation data freely available. We acknowledge the developers at NOAA ESRL that have maintained the C program of the ccgcrv algorithm and made it freely available. LC was supported by a National Aeronautics and Space Administration Earth and Space Science Fellowship (NASA ESSF 2016-2019). PKP acknowledges support from the Tougou (Theme B) project of the Ministry of Education, Culture, Sports, Science and Technology.

Author Contribution

LC, BP, and PKP conceived of the study. PKP conducted the atmospheric simulations. LC prepared and analyzed simulated and satellite data. LC developed the code for the segmentation algorithm. LC prepared the manuscript with contributions from all co-authors.

Data Availability

Data used in the analysis and code for the segmentation algorithm is freely-available from the GitHub repository <https://github.com/lcalle/segmentTS>. The permanent version of the algorithm is archived and freely available at the Dryad Digital Repository < doi:10.5061/dryad.vk8ms62>.

References

Anav, A., Friedlingstein, P., Beer, C., Ciais, P., Harper, A., Jones, C., Murray-Tortarolo, G., Papale, D., Parazoo, N. C., Peylin, P., Piao, S., Sitch, S., Viovy, N., Wiltshire, A., & Zhao, M.: Spatiotemporal patterns of terrestrial gross primary production – a review. Reviews of Geophysics, 53, 785-818. doi:10.1002/2015RG000483, 2015.

Arneth, A., Sitch, S., J. Pongratz, Stocker, B. D., Ciais, P., Poulter, B., Bayer, A. D., Bondeau, A., Calle, L., Chini, L. P., Gasser, T., Fader, M., Friedlingstein, P., Kato, E., Li, W., Lindeskog, M., Nabel, J. E. M. S., Pugh, T. A. M., Robertson, E., Viovy, N., Yue, C., & Zaehle, S.: Historical carbon dioxide emissions caused by land-use changes are possibly larger than assumed. Nature Geoscience, 10. doi: 10.1038/NGEO2882, 2017.

Bagley, J. E., Desai, A. R., Harding, K. J., Snyder, P. K. & Foley, J. A.: Drought and deforestation – Has land cover change influence recent precipitation extremes in the Amazon? Journal of Climate 27:345-361, doi: 10.1175/JCLI-D-12-00369.1, 2014.

Belikov, D. A., Maksyutov, S., Ganshin, A., Zhuravlev, R., Deutscher, N. M., Wunch, D., Feist, D. G., Morino, I., Parker, R. J., Strong, K., Yoshida, Y., Bril, A., Oshchepkov, S., Boesch, H., Dubey, M. K., Griffith, D., Hewson, W., Kivi, R., Mendonca, J., Notholt, J., Schneider, M., Sussmann, R., Velazco, V. A. & Aoki, S. (2017). Atmospheric Chemistry and Physics 17:143-157, doi: 10.5194/acp-17-143-2017.

Betts, A. K., Desjardins, R., Worth, D. & Cerkowniak, D.: Impact of land use change on the diurnal cycle climate of the Canadian Prairies. Journal of Geophysical Research – Atmospheres 188(11):996-12011, doi: 10.1002/2013JD020717, 2013.

Bonan, G. B.: Forests and climate change – forcings, feedbacks, and the climate benefits of forests. Science, 320,

600   1444. doi: 10.1126/science.1155121, 2008.

Calle, L., Canadell, J. G., Patra, P. K., Ciais, P., Ichii, K., Tian, H., Kondo, M., Piao, S., Arneth, A., Harper, A. B., Ito, A., Kato, E., Koven, C., Sitch, S., Stocker, B. D., Vivoy, N., Wiltshire, A., Zaehle, S., and Poulter, B.: Regional carbon fluxes from land use and land cover change in Asia, 1980-2009. Environmental Research Letters 11:074011, 2016.

605   Ciais, P., Dolman, A. J., Bombelli, A., Duren, R., Peregon, A., Rayner, P. J., Miller, C., Gobron, N., Kinderman, G., Marland, G., Gruber, N., Chevallier, F., Andres, R. J., Balsamo, G., Bopp, L., Bréon, F.-M., Broquet, G., Dargaville, R., Battin, T. J., Borges, A., Bovensmann, H., Buchwitz, M., Butler, J., Canadell, J. G., Cook, R. B., DeFries, R., Engelen, R., Gurney, K. R., Heinze, C., Heimann, M., Held, A., Henry, M., Law, B., Luyssaert, S., Miller, J., Moriyama, T., Moulin, C., Myneni, R. B., Nussli, C., Obersteiner, M., Ojima, D., Pan, Y., Paris, J.-
610   D., Piao, S. L., Poulter, B., Plummer, S., Quegan, S., Raymond, P., Reichstein, M., Rivier, L., Sabine, C., Schimel, D., Tarasova, O., Valentini, R., Wang, R., van der Werf, G., Wickland, D., Williams, M. & Zehner, C.: Current systematic carbon-cycle observations and the need for implementing a policy-relevant carbon observing system. Biogeosciences, 11, 3547-3602, doi: 10.5194/bg-11-3547-2014, 2015.

Crisp, D., Fisher, B. M., O'Dell, C. O., Frankenberg, C., Basilio, R., Bösch, H., Brown, L. R., Castano, R., Conner,
615   B., Deutscher, N. M., Eldering, A., Griffith, D., Gunson, M., Kuze, A., Mandrake, L., McDuffie, J., Messerschmidt, J., Miller, C. E., Morino, I., Natraj, V., Notholt, J., O'Brien, D. M., Oyafuso, F., Polonsky, I., Robinson, J., Salawitch, R., Sherlock, V., Smyth, M., Suto, H., Taylor, T. E., Thompson, D. R., Wennberg, P. O., Wunch, D., & Yung, Y. L.: The ACOS CO_2 retrieval algorithm – Part II – Global XCO_2 data characterization. Atmospheric Measurement Techniques, 5, 687-707. doi:10.5194/amt-5-687-2012, 2012.

620   Earles, J. M., Yeh, S. & Skog, K. E.: Timing of carbon emissions from global forest clearance. Nature Climate Change 2:682-685, doi:10.1038/NCLIMATE1535, 2012.

Ehret, U., & Zehe, E.: Series distance – an intuitive metric to quantify hydrograph similarity in terms of occurrence, amplitude and timing of hydrological events. Hydrology and Earth Systems Science, 15, 877-896. doi:10.5194/hess-15-877-2011, 2011.

625   Fisher, R. A., Koven, C. D., Anderegg, W. R. L., Christoffersen, B. O., Dietze, M. C., Farrior, C. E., Holm, J. A., Hurtt, G. C., Knox, R. G., Lawrence, P. J., Lichstein, J. W., Longo, M., Matheny, A. M., Medvigy, D., Muller-Landau, H. C., Powell, T. L., Serbin, S. P., Sato, H., Shuman, J. K., Smith, B., Trugman, A. T., Viskari, T., Verbeeck, H., Wang, E., Xu, C., Xu, X., Zhang, T., Moorcroft, P. R.: Vegetation demographics in Earth System Models – A review of progress and priorities. Global Change Biology 24:35-54, doi:10.1111/gcb.13910, 2018.

630   Fleishcher, E., Khashimov, I., Hölzel, N. & Klemm, O.: Carbon exchange fluxes over peatlands in Western Siberia – possible feedback between land-use change and climate change. Science of the Total Environment, doi: 10.1016/j.scitotenv.2015.12.073, 2016.

Forkel, M., Carvalhais, N., Schaphoff, S., Bloh, W. v., Migliavacca, M., Thurner, M., & Thonicke, K.: Identifying environmental controls on vegetation greenness phenology through model-data integration. Biogeosciences, 11,
635   7025-7050. doi:10.5194/bg-11-7025-2014, 2014.

Fu, Z., Dong, J., Zhou, Y., Stoy, P. C. & Niu, S.: Long term trend and interannual variability of land carbon uptake –

the attribution and processes. Environmental Research Letters 12: 014018, doi: 10.1088/1748-9326/aa5685, 2017.

Glecker, P. J., Taylor, K. E., & Doutriaux, C.: Performance metrics for climate models. Journal of Geophysical Research - Atmospheres, 113, D06104. doi:10.1029/2007/JD008972, 2008.

Goldewijk, K. K., Beusen, A., van Drecht, G., & de Vos, M.: The HYDE 3.1 spatially explicit database of human-induced global land-use change over the past 12,000 years. Global Ecology and Biogeography., 20, 73-86. doi: 10.1111/j.1466-8238.2010.00587.x, 2011.

Guerlet, S., Butz, A., Schepers, D., Basu, S., Hasekamp, O. P., Kuze, A., Yokota, T., Blavier, J. F., Deutscher, N. M., Grif- fith, D. W. T., Hase, F., Kyro, E., Morino, I., Sherlock, V., Suss- mann, R., Galli, A., and Aben, I.: Impact of aerosol and thin cirrus on retrieving and validating XCO_2 from GOSAT shortwave infrared measurements. Journal Geophysical Research - Atmospheres, 118, 4887– 4905, https://doi.org/10.1002/jgrd.50332, 2013.

Hammerling, D. M., Kawa, S. R., Schaefer, K., Doney, S. & Michalak, A. M.: Detectability of CO_2 flux signals by a space-based lidar mission. Journal of Geophysical Research – Atmospheres 120, 1794–1807, doi:10.1002/2014JD022483, 2015.

Jones, C. D. & Cox, P. M.: Modeling the volcanic signal in the atmospheric CO_2 record. Global Biogeochemical Cycles 15(2):452-465, 2001.

Kato, E., Kinoshita, T., Ito, A., Kawamiya, M., & Yamagata, Y.: Evaluation of spatially explicit emission scenario of land-use change and biomass burning using a process-based biogeochemical model. Journal of Land Use Science, 8:1, 104-122. doi: 10.1080/1747423X.2011.628705, 2013.

Keeling, C. D., Whorf, T. P., Wahlen, M., & van der Plicht, J.: Interannual extremes in the rate of rise of atmospheric carbon dioxide since 1980. Nature, 375, 666-670, 1995.

Krinner, G., Viovy, N., de Noblet-Ducoudré, N., Ogeé, J., Polcher, J., Friedlingstein, P., Ciais, P., Sitch, S., & Prentice, I. C.: A dynamic global vegetation model for studies of the coupled atmosphere–biosphere system. Global Biogeochemical Cycles, 19, GB1015. doi:10.1029/2003GB002199, 2005.

Lawrence, D. M., Oleson, K. W., Flanner, M. G., Thornton, P. E., Swenson, S. C., Lawrence, P. J., Zeng, X., Yang, Z. L., Levis, S., Sakaguchi, K., Bonan, G. B., & Slater, A. G.: Parameterization improvements and functional and structural advances in version 4 of the Community Land Model. Journal of Advances in Modeling Earth Systems, 3, M03001. doi:10.1029/2011MS000045, 2011.

Le Quéré, C., Andrew, R. M., Friedlingstein, P., Sitch, S., Pongratz, J., Manning, A. C., Korsbakken, J. I., Peters, G. P., Canadell, J. G., Jackson, R. B., Boden, T. A., Tans, P. P., Andrews, O. D., Arora, V. K., Bakker, D. C. E., Barbero, L., Becker, M., Betts, R. A., Bopp, L., Chevallier, F., Chini, L. P., Ciais, P., Cosca, C. E., Cross, J., Currie, K., Gasser, T., Harris, I., Hauck, J., Haverd, V., Houghton, R. A., Hunt, C. W., Hurtt, G. C., Ilyina, T., Jain, A. K., Kato, E., Kautz, M., Keeling, R. F., Goldewijk, K. K., Körtzinger, Landschützer, P., Lefèvre, N., Lenton, A., Lienert, S., Lima, I., Lombardozzi, D., Metzl, N., Millero, F., Monteiro, P. M. S., Munro, D. R., Nabel, J. E. M. S., Nakaoka, S., Nojiri, Y., Padin, X. A., Peregon, A., Pfeil, B., Pierrot, D., Poulter, B., Rehder, G., Reimer, J., Rödenbeck, C., Schwinger, J., Séférian, R., Skjelvan, I., Stocker, B. D., Tian, H., Tilbrook, B.,

Tubiello, F. N., van der Laan-Luijkx, I. T., van der Werf, G. R., van Heuven, S., Viovy, N., Vuichard, N., Walker, A. P., Watson, A. J., Wiltshire, A. J., Zaehle, S. & Zhu, D.: Global Carbon Budget, Earth System Science Data, 10, 405-448, doi: 10.5194/essd-10-405-2018, 2018.

Lindqvist, H., O'Dell, C. W., Basu, S., Boesch, H., Chevallier, F., Deutscher, N., Feng, L., Fisher, B., Hase, F., Inoue, M., Kivi, R., Morino, I., Palmer, P. I., Parker, R., Schneider, M., Sussmann, R., and Yoshida, Y.: Does GOSAT capture the true seasonal cycle of carbon dioxide?, Atmospheric Chemistry and Physics, 15, 13023–13040, https://doi.org/10.5194/acp-15-13023-2015, 2015.

Liptak, J., Keppel-Aleks, G. & Lindsay, K.: Drivers of multi-century trends in the atmospheric CO_2 mean annual cycle in a prognostic ESM. Biogeosciences 14:1383-1401, doi: 10.5194/bg-14-1383-2017, 2017.

Nakazawa, T., Ishizawa, M., Higuchi, K., & Trivett, N. B. A.: Two curve fitting methods applied to CO2 flask data. Environmetrics, 8, 197-218, 1997.

O'Dell, C. W., Conner, B., Bösch, H., O'Brien, D. O., Frankenberg, C., Castano, R., Christi, M., Crisp, D., Eldering, A., Fisher, B., Gunson, M., McDuffie, J., Miller, C. E., Natraj, V., Oyafuso, F., Polonsky, I., Smyth, M., Taylor, T., Toon, G. C., Wennberg, P. O., & Wunch, D.: The ACOS CO_2 retrieval algorithm – Part 1 – Description and validation against synthetic observations. Atmospheric Measurement Techniques, 5, 99-121. doi:10.5194/amt-5-99-2012, 2012.

Olsen, S. C. & Randerson, J. T. Differences between surface and column atmospheric CO_2 and implications for carbon cycle research. Journal of Geophysical Research 109:D02301, doi: 10.1029/2003JD003968, 2004.

Parazoo, N. C., Commane, R., Wofsy, S. C., Koven, C. D., Sweeney, C., Lawrence, D. M., Lindaas, J., Chang, R. Y.-W., & Miller C. E.: Detecting regional patterns of changing CO_2 flux in Alaska. Proceedings of the National Academies of Science, 113, 7733-7738, doi:10.1073/pnas.1601085113, 2016.

Patra, P. K., Takigawa, M., Dutton, G. S., Uhse, K., Ishijima, K., Lintner, B. R., Miyazaki, K., & Elkins, J. W.: Transport mechanisms for synoptic, seasonal and interannual SF6 variations and 'age' of air in troposphere. Atmospheric Chemistry and Physics, 9, 1209-1225, 2009.

Peng, S., Ciais, P., Chevallier, F., Peylin, P., Cadule, P., Sitch, S., Piao, S., Ahlström, A., Huntingford, C., Levy, P., Li, X., Liu, Y., Lomas, M., Pouler, B., Viovy, N., Wang, T., Wang, X., Zaehle, S., Zeng, N., Zhao, F., & Zhao, H.: Benchmarking the seasonal cycle of CO2 fluxes simulated by terrestrial ecosystem models. Global Biogeochemical Cycles, 29, 46-64. doi:10.1002/2014GB004931, 2015.

Pickers, P. A., & Manning, A. C.: Investigating bias in the application of curve fitting programs to atmospheric time series. Atmospheric Measurement Techniques, 8, 1469-1489. doi:10.5194/amt-8-1469-2015, 2015.

Pongratz, J., Reick, C. H., Houghton, R. A. & House, J. I.: Terminology as a key uncertainty in net land use and land cover change flux estimates. Earth System Dynamics 5:177-195, doi:10.5194/esd-5-177-2014, 2014.

Poulter, B., Ciais, P., Hodsen, E., Lischke, H., Maignan, F., Plummer, S., & Zimmermann, N. E.: Plant functional type mapping for earth system models. Geoscientific Model Development, 4, 993-1010. doi:10.5194/gmd-4-993-2011, 2011.

Prentice, I. C., Kelley, D. I., Foster, P. N., Friedlingstein, P., Harrison, S. P., & Bartlein, P. J.: Modeling fire and the terrestrial carbon balance. Global Biogeochemical Cycles 25:GB3005, 2011.

Pugh, T. A. M., Müller, C., Arneth, A., Haverd, V. & Smith, B.: Key knowledge and data gaps in modelling the influence of CO_2 concentration on the terrestrial carbon sink. Journal of Plant Physiology 203:3-15, 2016.

R Development Core Team. R: A language and environment for statistical computing. R Foundation for Statistical Computing, Vienna, Austria. ISBN 3-900051-07-0, URL http://www.R-project.org., 2008.

715   Randerson, J. T., Thompson, M. V., Conway, T. J., Fung, I. Y. & Field, C. B.: The contribution of terrestrial sources and sinks to trends in the seasonal cycle of atmospheric carbon dioxide. Global Biogeochemical Cycles 11(4):535-560, 1997.

Richardson, A. D., Anderson, R. S., Arain, M. A., Barr, A. G., Bohrer, G., Chen, G., Chen, J. M., Ciais, P., Davis, K. J., Desai, A. R., Dietze, M. C., Dragnoi, D., Garrity, S. R., Gough, C. M., Grant, R., Hollinger, D. Y.,

720   Margolis, H. A., McCaughey, H., Migliavacca, M., Monson, R. K., Munger, J. W., Poulter, B., Raczka, B. M., Ricciuto, D. M., Sahoo, A. K., Schaefer, K., Tian, H., Vargas, R., Verbeeck, H., Xiao, J., & Xue, Y.: Terrestrial biosphere models need better representation of vegetation phenology – results from the North American Carbon Program site synthesis. Global Change Biology, 18, 566-584. doi:10.1111/j.1365-2486.2011.02562.x, 2012.

Saeki, T. & Patra, P. K.: Implications of overestimated anthropogenic CO_2 emissions on East Asian and global land

725   CO_2 flux inversion. Geoscience Letters 4:9, doi:10.1186/s40562-017-0074-7, 2017.

Saito, R., Patra, P. K., Deutscher, N., Wunch, D., Ishijima, K., Sherlock, V., Blumenstock, T., Dohe, S., Griffith, D., Hase, F., Heikkinen, P., Kyro, E., Macatangay, R., Mendonca, J., Messerschmidt, J., Morino, I., Notholt, J., Rettinger, M., Strong, K., Sussmann, R. & Warneke, T.: Technical Note – Latitude-time variations of atmospheric column-average dry air mole fractions of CO2, CH4, N2O. Atmospheric Chemistry and Physics

730   12:7767-7777, doi:10.5194/acp-12-7767-2012, 2012.

Schneising, O., Reuter, M., Buchwitz, M., Heymann, J., Bovensmann, H. & Burrows, J. P.: Terrestrial carbon sink observed from space – variation of growth rates and seasonal cycle amplitudes in response to interannual surface temperature variability. Atmospheric Chemistry and Physics 14:133-141, doi: 10.5194/acp-14-133-2014, 2014.

735   Sitch, S., Smith, B., Prentice, I. C., Arneth, A., Bondeau, A., Cramer, W., Kaplan, J. O., Levis, S., Lucht, W., Sykes, M. T., Thonicke, K., & Venevsky, S.: Evaluation of ecosystem dynamics, plant geography and terrestrial carbon cycling in the LPJ dynamic global vegetation model. Global Change Biology 9:161–185, 2003.

Sitch, S., Friedlingstein, P., Grubber, N., Jones, S. D., Murray-Tortarolo, G., Ahlström, A., Doney, S. C., Graven, H., Heinze, C., Huntingford, C., Levis, S., Levy, P. E., Lomas, M., Poulter, B., Viovy, N., Zaehle, S., Zeng, N.,

740   Arneth, A., Bonan, G., Bopp, L., Canandell, J. G., Chevallier, F., Ciais, P., Ellis, R., Gloor, M., Peylin, P., Piao, S. L., Le Quére, C., Smith, B., Zhu, Z., and Myneni, R.: Recent trends and drivers of regional sources and sinks of carbon dioxide. Biogeosciences, 12, 653-679. doi:10.5194/bg-12-653-2015, 2015.

Smith, B., Prentice, I. C., & Sykes, M. T.: Representation of vegetation dynamics in the modelling of terrestrial ecosystems: comparing two contrasting approaches within European climate space. Global Ecology and

745   Biogeography 10:621–638, 2001.

Sweeney, C., Karion, A., Wolter, S., Newberger, T., Guenther, D., Higgs, J. A., Andrews, A. E., Lang, P. M., Neff, D., Dlugokencky, E., Miller, J. B., Montzka, S. A., Miller, B. R., Masarie, K. A., Biraud, S. C., Novelli, P. C.,

Crotwell, M., Crotwell, A. M., Thoning, K. & Tans, P. P. (2015). Seasonal climatology of CO_2 across North America from aircraft measurements in the NOAA/ESRL Global Greenhouse Gas Reference Network. Journal of Geophysical Research - Atmospheres 120:5155–5190, doi:10.1002/ 2014JD022591, 2015.

Taylor, K. E.: Summarizing multiple aspects of model performance in a single diagram. Journal of Geophysical Research - Atmospheres, 106, 7183-7192, 2001.

Thoning, K. W., Tans, P. P., & Komhyr, W. D.: Atmospheric carbon dioxide at Mauna Loa Observatory, 2. Analysis of the NOAA CMCC data, 1974-1985. Journal of Geophysical Research, 94, 8549-8565, 1989.

Wunch, D., Wennberg, P. O., Toon, G. C., Connor, B. J., Fisher, B., Osterman, G. B., Frankenberg, C., Mandrake, L., O'Dell, C., Ahonen, P., Biraud, S. C., Castano, R., Cressie, N., Crisp, D., Deutscher, N. M., Eldering, A., Fisher, M. L., Griffith, D. W. T., Gunson, M., Heikkinen, P., Keppel-Aleks, G., Kyro, E., Lindenmaier, R., Macatangay, R., Mendonca, J., Messerschmidt, J., Miller, C. E., Morino, I., Notholt, J., Oyafuso, F. A., Rettinger, M. A., Robinson, J., Roehl, C. M., Salawitch, R. J., Sherlock, V., Strong, K., Sussmann, R., Tanaka, T., Thompson, D. R., Uchino, O., Warneke, T., & Wofsy, S. C. A method for evaluating bias in global measurements of CO2 total columns from space. Atmospheric Chemistry and Physics, 11, 12317-12337, 2011.

Xia, J., Niu, S., Ciais, P., Janssens, I. A., Chen, J., Ammann, C., Arain, A., Blanken, P. D., Cescatti, A., Bonal, D., Buchmann, N., Curtis, P. S., Chen, S., Dong, J., Flanagan, L. B., Frankenberg, C., Georgiadis, T., Gough, C. M., Hui, D., Kiely, G., Li, J., Lund, M., Magliulo, V., Marcolla, B., Merbold, L., Montagnani, L, Moors, E. J., Olesen, J. E., Piao, S., Raschi, A., Roupsard, O., Suyker, A. E., Urbaniak, M., Vaccari, F. P., Varlagin, A., Vesala, T., Wilkinson, M., Weng, E., Wohlfahrt, G., Yan, L. & Luo, Y.: Joint control of terrestrial gross primary production by plant phenology and physiology. Proceedings of the National Academies of Science 112(9):2788-2793, doi: 10.1073/pnas.1413090112, 2015.

Yoshida, Y., Ota, Y., Eguchi, N., Kikuchi, N., Nobuta, K., Tran, H., Morino, I., and Yokota, T.: Retrieval algorithm for CO_2 and CH_4 column abundances from short-wavelength infrared spectral observations by the greenhouse gases observing satellite. Atmospheric Measurement and Techniques, 4, 717–734, doi:10.5194/amt-4-717-2011, 2011.

Zaehle, S., & Friend, A. D.: Carbon and nitrogen cycle dynamics in the O-CN land surface model: 1. Model description, site-scale evaluation, and sensitivity to parameter estimates. Global Biogeochemical Cycles, 24, GB1005. doi: 10.1029/2009GB003521, 2010.

Table 1. Terrestrial ecosystem models from the TRENDY v.2 model inter-comparison used to simulate terrestrial Net Ecosystem Exchange.

Model	Abbrev.	Spatial Resolution	Land Surface Model	Fire Simulation	C-N coupled cycle	Source
Community Land Model v.4.5	CLM	2.5 X 2.5	Yes	Yes	Yes	Lawrence et al. (2011)
Lund-Potsdam-Jena	LPJ	0.5 X 0.5	No	Yes	No	Sitch et al. (2003)
Land-surface Processes and exchanges	LPX	1.0 X 1.0	No	Yes	Yes	Prentice et al. (2011)
ORganizing Carbon and Hydrology in Dynamic EcosystEms	ORCHIDEE	3.74 X 2.5	Yes	Yes	No	Krinner et al. (2005)
ORCHIDEE with coupled C-N cycling	OCN	1.0 X 1.0	Yes	Yes	Yes	Zaehle and Friend (2010)
Vegetation Integrative SImulator for Trace gases	VISIT	0.5 X 0.5	No	Yes	Yes	Kato et al. (2013)

Table 2. Signal characteristics for Rise and Fall segments of the GOSAT-derived XCO₂ seasonal cycles (2009-2012) by TransCom region. The timeframe of one Rise plus one Fall segment approximately equates to one year. North America Boreal and South America Tropical regions were excluded for lack of observations to derive signals for Rise or Fall segments.

Region	Segment	Period (days)		Amplitude (ppm)	
		Fall	Rise	Fall	Rise
Africa Northern	1,2	118	241	5.4	6.1
	3,4	130	229	5.5	5.2
	5,6	135	232	6.0	5.8
	7	135	NA	5.7	NA
Africa Southern	1,2	174	216	2.5	3.0
	3,4	131	131	4.0	3.6
	5,6	218	147	3.2	3.0
Asia Tropical	1,2	NA	194	NA	6.4
	3,4	NA	200	NA	7.5
	5,6	NA	190	NA	7.0
Australia	1,2	140	225	2.0	1.2
	3,4	136	209	2.0	2.5
	5,6	155	228	2.4	2.4
Europe*	2,1	115	236	6.8	8.0
	3,4	131	239	7.9	6.4
	5,6	132	244	6.1	7.4
Eurasia Temperate*	2,1	109	248	6.2	7.1
	3,4	108	255	7.2	6.4
	5,6	118	253	5.7	6.5
Eurasia Boreal	1,2	102	NA	10.9	NA
	3,4	100	NA	11.7	NA
	5,6	104	NA	11.2	NA
North America Temperate	1,2	129	235	6.4	6.8
	3,4	126	243	5.6	5.4
	5,6	127	233	6.0	5.3
	7	129	NA	5.6	NA
South America Temperate	1,2	232	91	2.1	2.0
	3,4	238	137	2.2	2.4
	5,6	234	154	2.9	2.6

* the first differentiable segment is a Rise segment, starting approximately ~100+ days after the first segment in other regions because the initial drawdown (Fall segment) in the region is a partial or incomplete segment.

Table 3. The interannual variation (IAV) in XCO$_2$ seasonal cycle metrics, presented as the relative standard deviation (i.e., RSD or coefficient of variation) and the LUCeffect, defined as the change in the XCO$_2$ seasonal cycle metrics when land-use change is included in simulations, relative to simulations with only natural vegetation. The values for IAV and LUCeffect presented below are first calculated for each region and segment type (Rise, Fall), and then averaged over all regions, and models (for LUCeffect). The values for the phasing metrics (day of year, 'DOY') are calculated using the period as the divisor.

metric	GOSAT IAV (%)	LUCeffect (%)
amplitude	12.3	14.2
period	14.5	7.5
DOYstart	9.3	6.5
DOYend	7.5	6.8
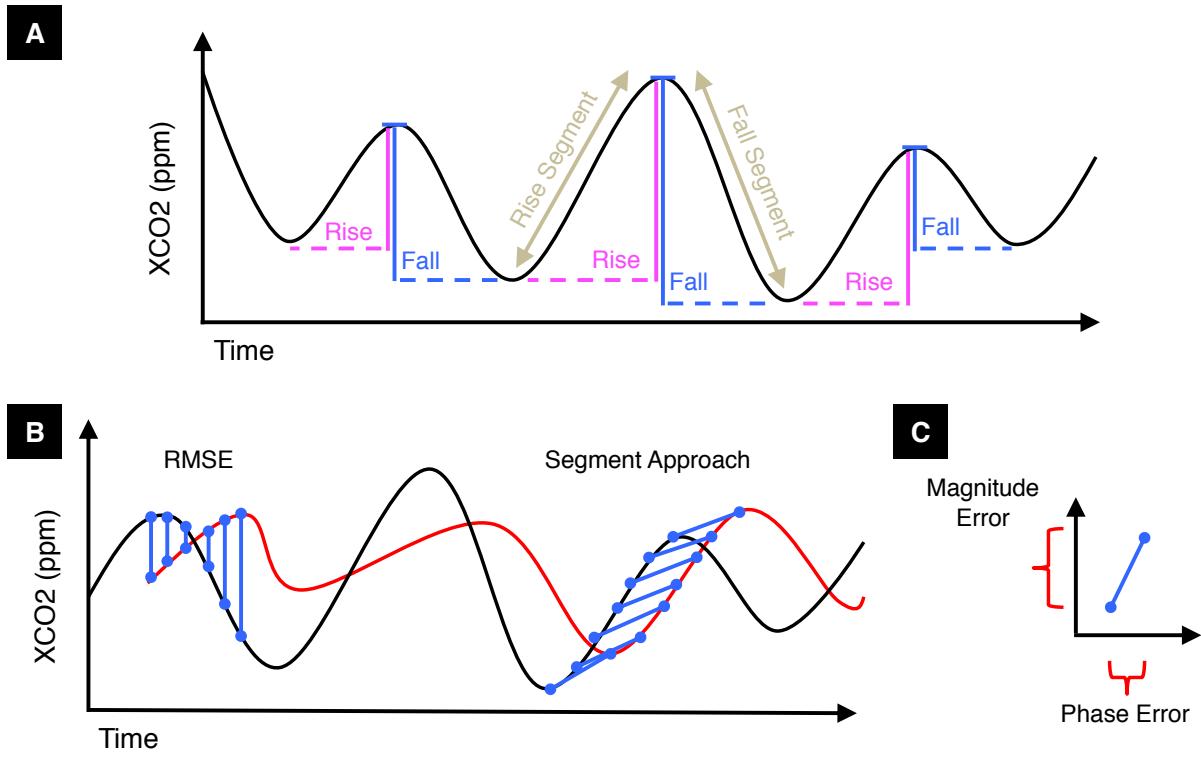
Figure 1. Conceptual diagram for the segmentation analysis. (A) interannual variation in seasonal cycle amplitudes (vertical, solid colored lines) and periods (horizontal, dashed colored lines); such interannual variation may also differ among Rise and Fall segments. (B) a reference (black) and a modeled seasonal cycle (red) are compared using the Root Mean Squared Error (RMSE), which is taken as the difference in magnitude at the same exact time in reference and modeled seasonal cycles; in out-of-phase signals, the RMSE misrepresents bias; the segmentation approach matches segments in the reference and modeled seasonal cycles, Rise-to-Rise and Fall-to-Fall, so that the errors in magnitude and phase can be decomposed and directly represented (C).
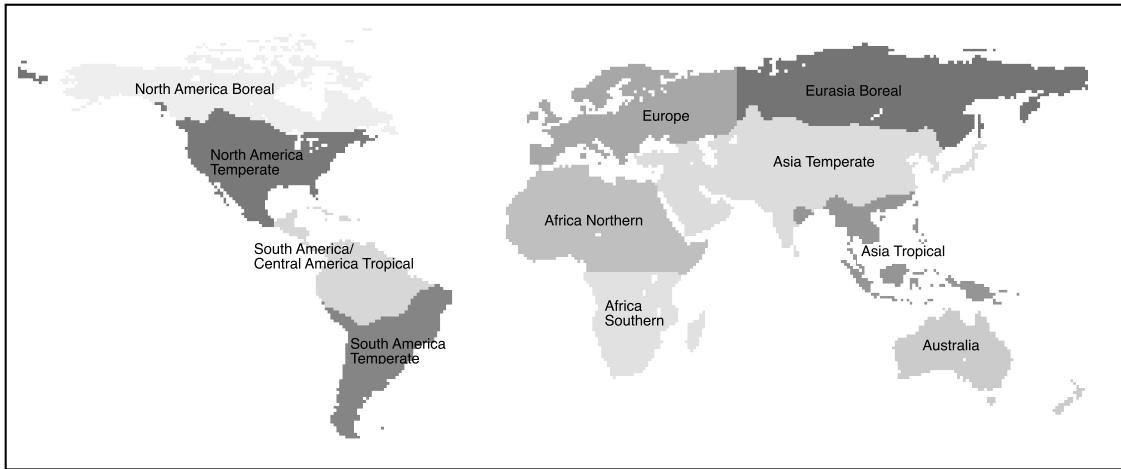
Figure 2. TransCom region map.
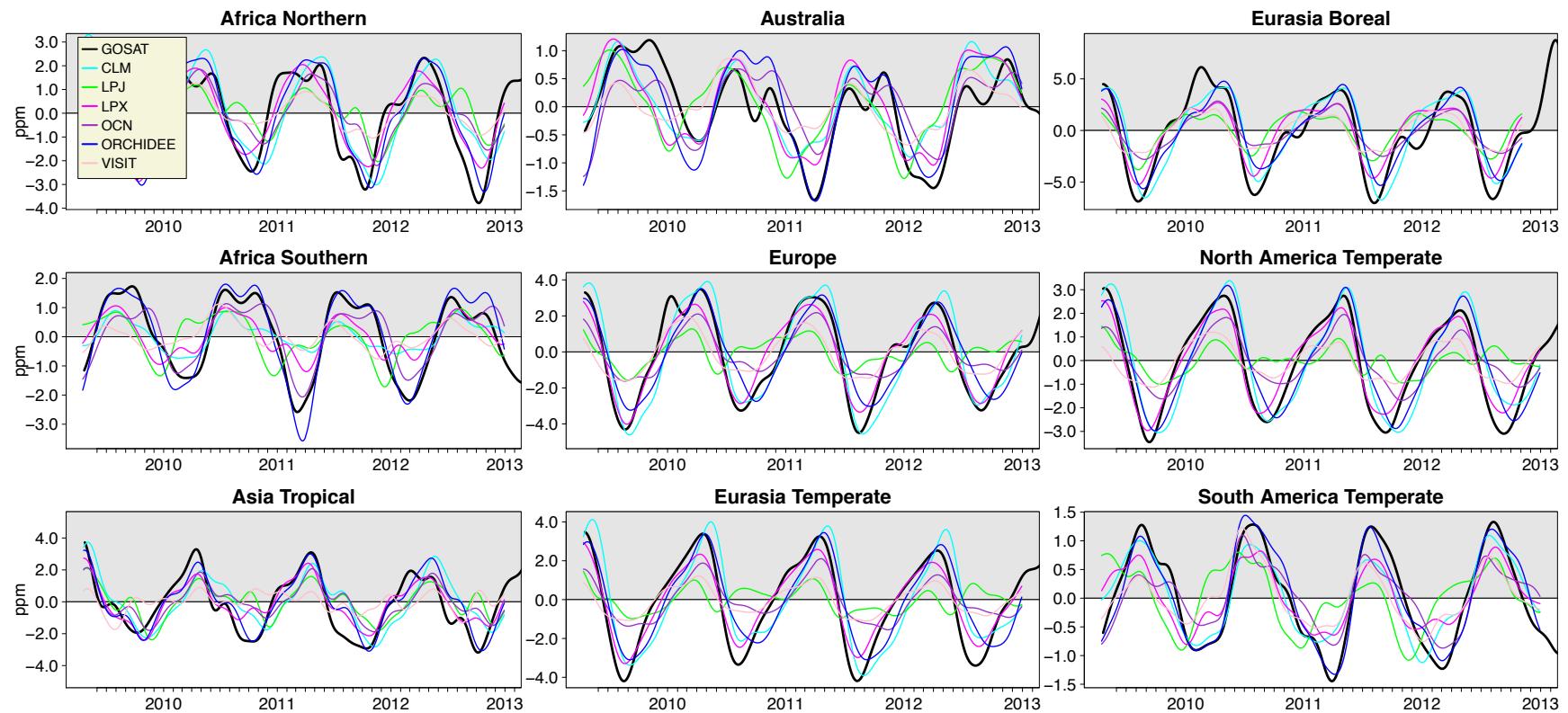
Figure 3. Detrended XCO₂ seasonal cycles by TransCom region. Simulated seasonal cycles are the sum of transported fluxes from DGVM, Fossil Fuel and Ocean, but only the DGVM model name is listed.
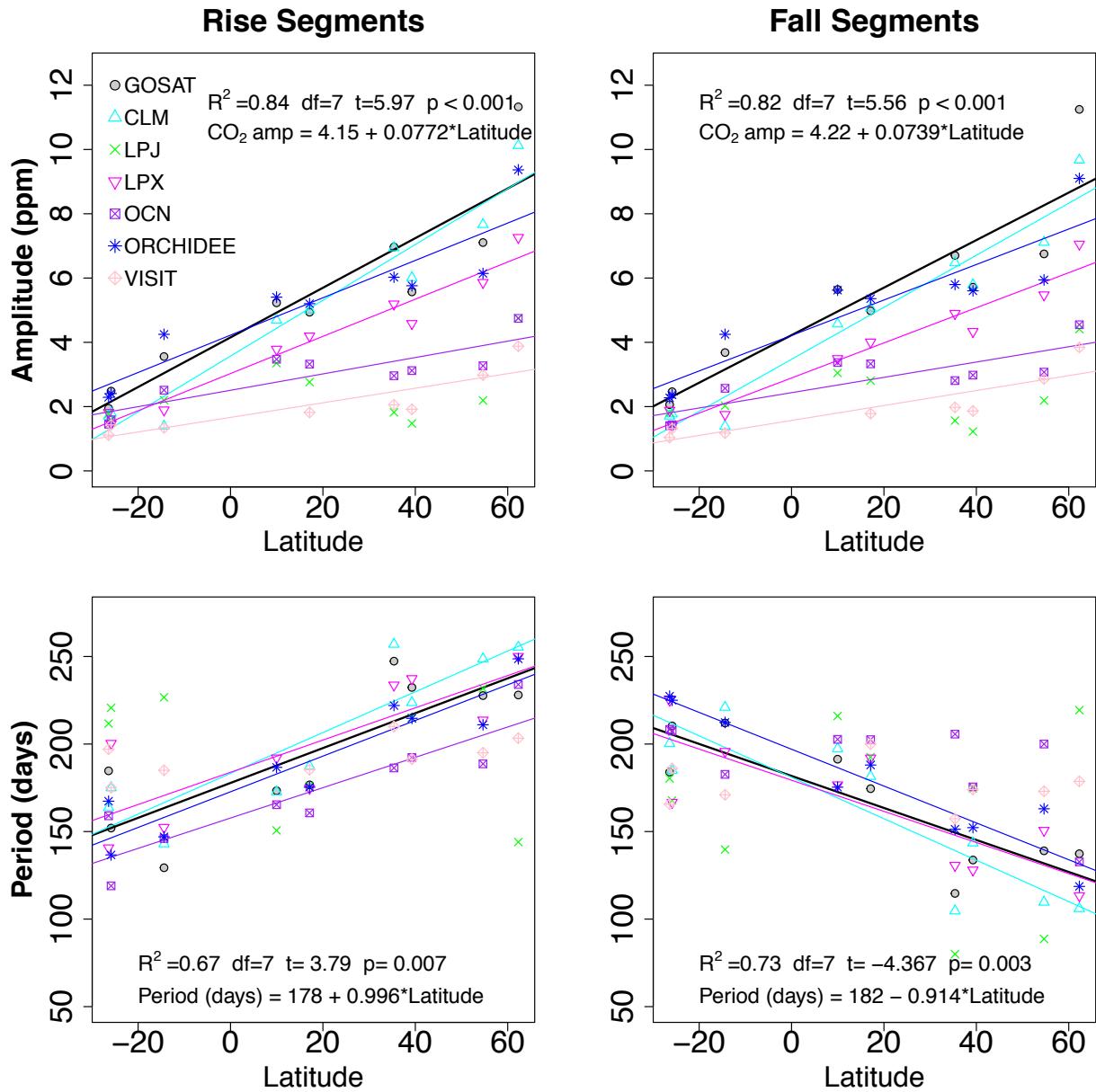
Figure 4. Latitudinal variation in amplitude and period in Rise and Fall segments among TransCom regions, using the average latitude for each region. Linear regressions shown when significant (p < 0.05). Regression statistics and equation only given for GOSAT.
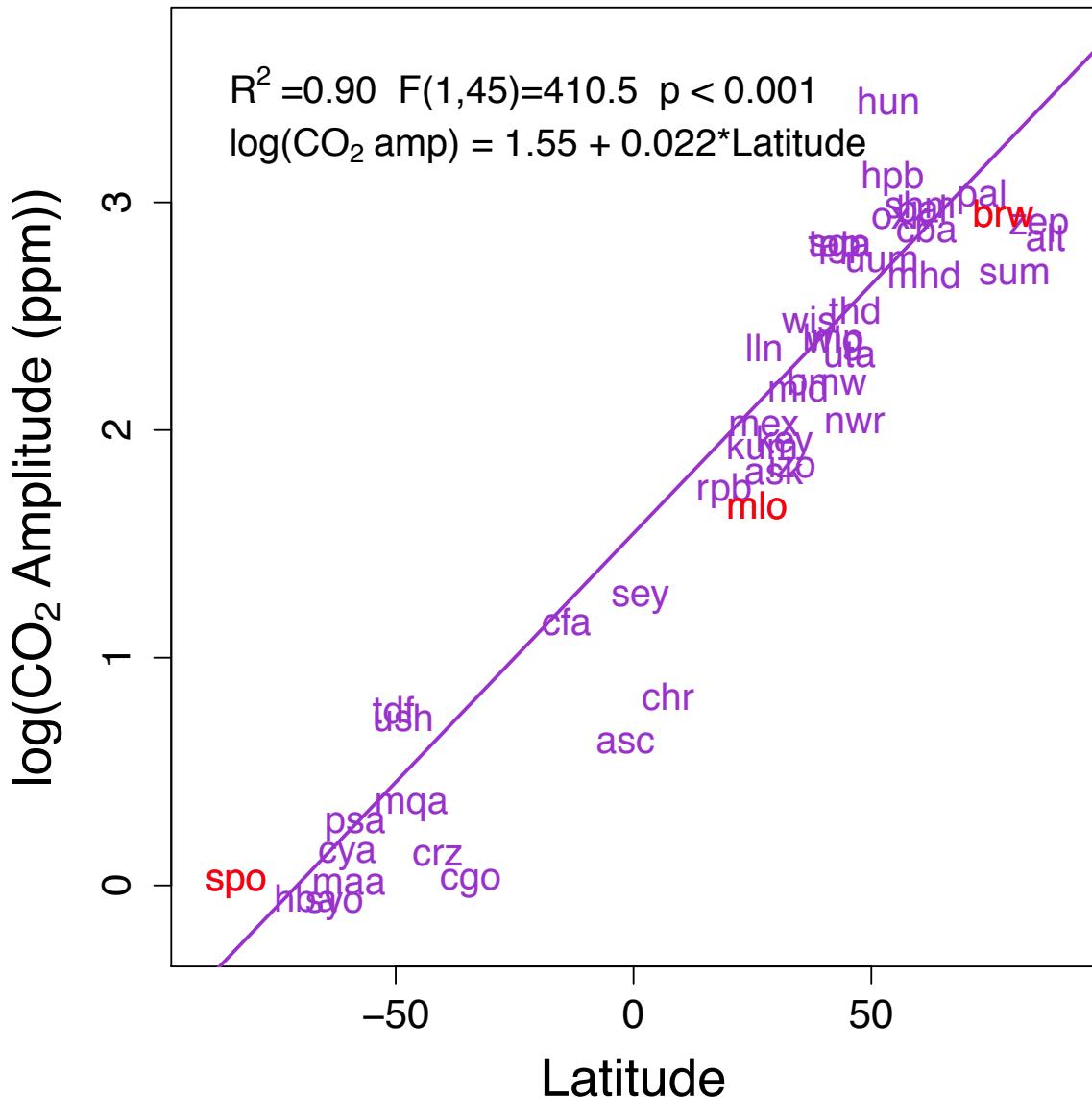
Figure 5. Latitudinal variation in the amplitude for detrended in-situ surface CO₂ samples. Data are the average of peak-trough amplitudes for 2005-2015, only including sites with a minimum of 5 years of data. Points are labeled according to the three-letter code of the sampling station. South Pole (spo), Mauna Loa (mlo), and Barrow Island (brw) are highlighted in red for reference as these sites are commonly referenced in literature. The latitudinal range in surface site CO₂ seasonal amplitudes (~ 19 ppm), is more than 2 times the latitudinal range in seasonal amplitudes of XCO₂.
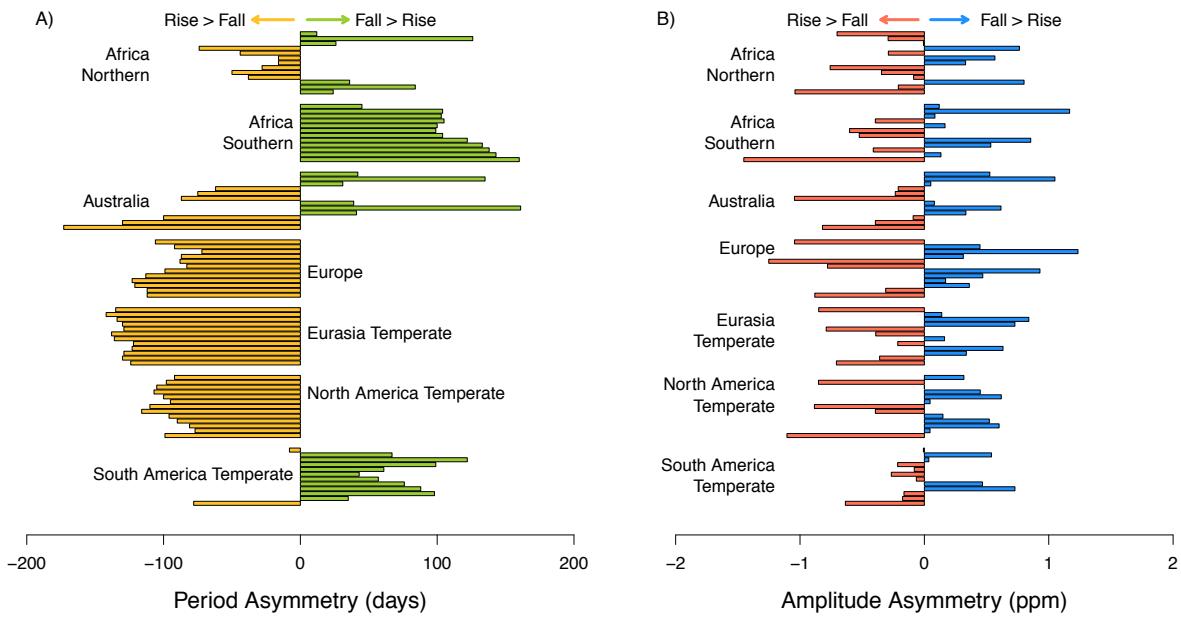
Figure 6. Period asymmetries (A) and Amplitude asymmetries (B) in GOSAT XCO₂ seasonal cycles. The bars represent differences in amplitude or period for consecutive Fall (F) and Rise (R) segments, taking the Fall segment as reference. For example, if the time series follows the sequence F1, R1, F2, R2, F3, R3, (i.e., 3 seasonal cycles), then the difference between the first segment (F1) and the second segment (R2) is calculated as 'F1-R2'; a zero value would indicate that the metric (amplitude or period) were equal, whereas an asymmetry would be indicated by a positive (F1 > R2) or negative (F1 < R2) value. By definition, consecutive segments cannot be categorized as F-F or R-R. Asymmetry statistics are not traditional summaries, but nevertheless, they are characteristic and in some regions persistent patterns of the seasonal cycle that are undoubtedly influenced by biosphere activity.
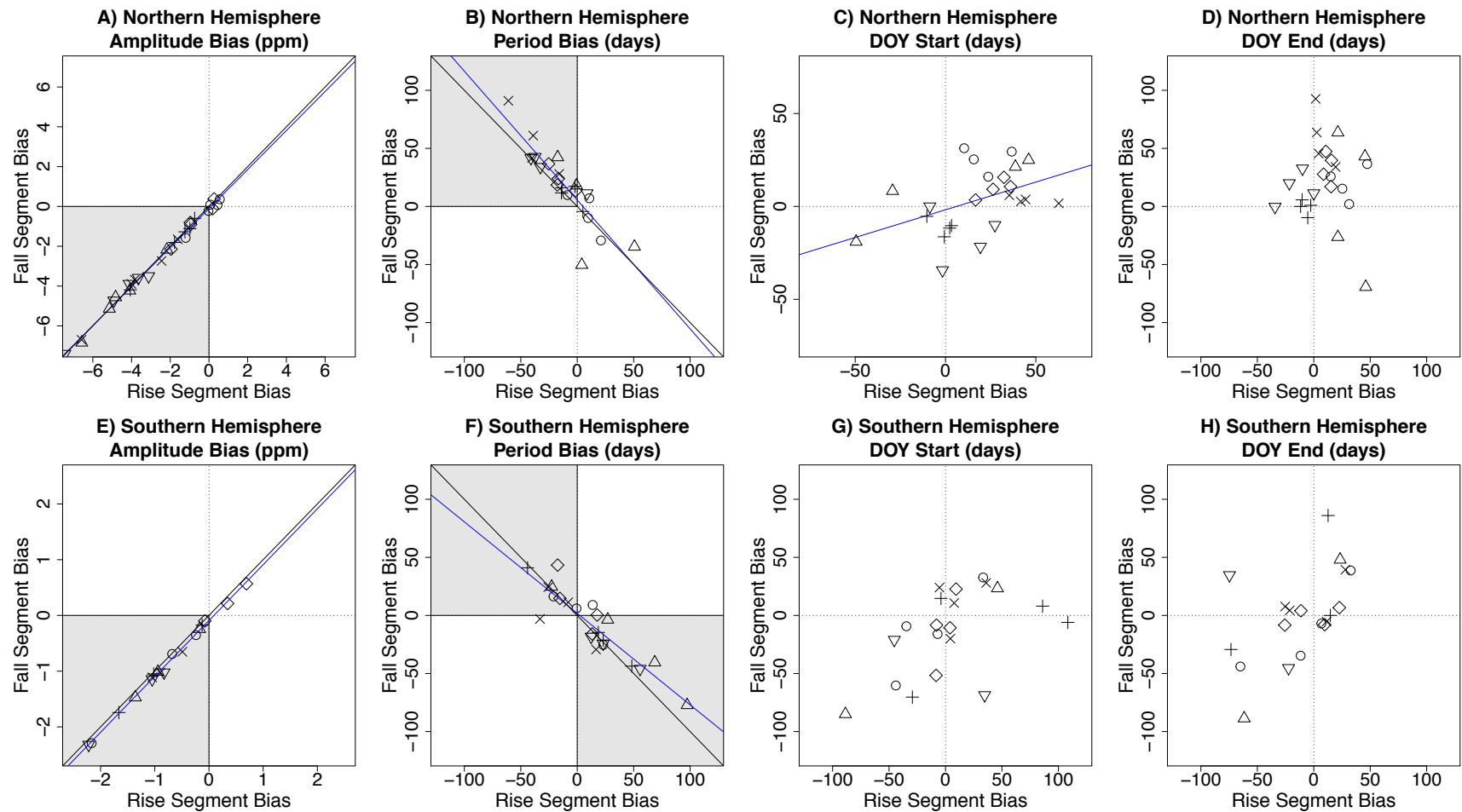
Figure 7. Emergent correlations among biases for Rise (x-axes) and Fall (y-axes) segments model biases, using GOSAT XCO₂ as reference, for TransCom regions in the Northern Hemisphere (top row) and Southern Hemisphere (bottom row). Data points are the average bias by model (unique symbols, not shown) for a particular region. Data for the Eurasia Boreal and Asia Tropical regions were excluded for lack of data in both Rise and Fall segments. Diagonal black lines are the 1:1 correspondence lines, blue lines are significant linear correlations.
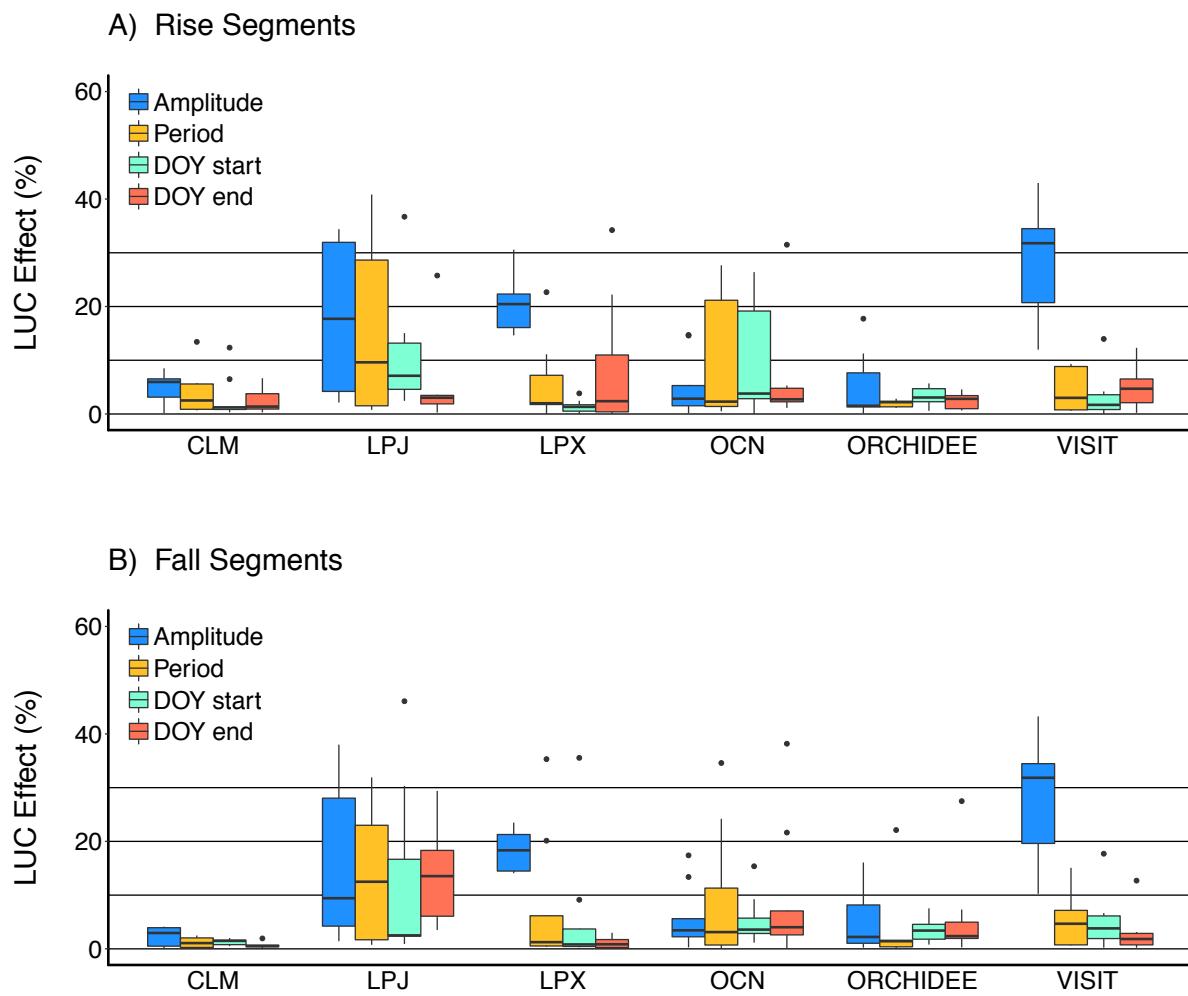
Figure 8. Land Use Change effect on amplitude, period, and day of year (DOY). The percentages were calculated from the difference in the metrics between simulations (S3-S2), scaled relative to amplitude and period of Rise and Fall segments for each region and model; DOY was scaled against the period.